Chemical Engineering Journal 452 (2023) 139474

Contents lists available at ScienceDirect

Chemical Engineering Journal

journal homepage: www.elsevier.com/locate/cej

# An injectable, self-healing composite hydrogel with enhanced near-infrared photo-antibacterial therapeutic effects for accelerated wound healing

Jiameng Wang [a], Hao Cheng [a], Weiyi Chen [b], Peide Han [c], Xiaohong Yao [a,*], Bin Tang [a], Wangping Duan [d], Pengcui Li [d], Xiaochun Wei [d], Paul K. Chu [e], Xiangyu Zhang [a,b,d,*]

[a] Shanxi Key Laboratory of Biomedical Metal Materials, College of Materials Science and Engineering, Taiyuan University of Technology, Taiyuan 030024, China
[b] College of Biomedical Engineering, Taiyuan University of Technology, Taiyuan 030024, China
[c] College of Materials Science and Engineering, Taiyuan University of Technology, Taiyuan 030024, China
[d] Shanxi Key Laboratory of Bone and Soft Tissue Injury Repair, Department of Orthopedics, Second Hospital of Shanxi Medical University, Taiyuan 030001, China
[e] Department of Physics, Department of Materials Science and Engineering, and Department of Biomedical Engineering, City University of Hong Kong, Tat Chee Avenue, Kowloon, Hong Kong, China

ARTICLE INFO

*Keywords:*
Hybrid hydrogel
CuS
P-n junction
Antibacterial activity
Wound healing

ABSTRACT

Antibacterial hydrogels with injectable and self-healing properties have attracted much attention in the field of wound dressings because they not only can prevent bacterial infections, but also meet the basic needs for wound healing. However, how to achieve high antibacterial efficacy and low drug resistance for hydrogels is still a challenge. Herein, an injectable, self-healing, near-infrared (NIR) photosensitive antibacterial hydrogel composed of CuS-grafted-curcumin (CuS@C) and carboxymethyl cellulose modified with aldehyde groups and hydroxypropyl trimethyl ammonium chloride chitosan is prepared for wound dressings. The p-n junction formed between curcumin and CuS promotes separation of electron-hole pairs, enhances the mobility of photogenerated charges, and destroys the conjugated structure of curcumin simultaneously consequently increasing the photocatalytic activity. CuS@C is immobilized and distributed uniformly in the hydrogel *via* the π-π conjugation ring. The hybrid hydrogel exhibits excellent antibacterial activity after irradiation with 808 NIR light for 10 min due to the enhanced photodynamic and photothermal antibacterial effects. In addition, the hybrid structure improves the biocompatibility of CuS and expedites infected-wound healing at a mild temperature of 45 ℃. This organic/inorganic hybrid is shown to be an excellent wound dressing for the treatment of bacterial-infected wounds.

## 1. Introduction

In recent years, drug-resistant bacteria caused by abuse of antibiotics have become one of the severe threats for wound treatment [1–3]. Light-controlled antibacterial hydrogels constitute a promising alternative to wound dressings due to the high antibacterial efficiency without bacterial resistance [4,5]. The common method to prepare light-controlled antibacterial hydrogels is to add inorganic photosensitive materials to hydrogels. For instance, Liu et al. have reported that polydopamine (PDA)-coated Au nanorods and *N*-acryloylglycinamide can form hydrogels by adding ammonium persulfate. The hydrogel can kill bacteria by generating reactive oxygen species (ROS) and hyperthermia upon irradiation with the 808 nm laser [6].

CuS nanospheres have been widely used in biomedicine on account of the low toxicity and good photostability [7–10]. CuS as a narrow bandgap p-type semiconductor exhibits photothermal and photodynamic effects upon NIR light illumination [11,12]. Furthermore, the biodegradability of CuS prevents the nanospheres from remaining in the human body as foreign matters [13–15]. However, the narrow bandgap of CuS leads to rapid recombination of photogenerated electrons and holes, resulting in limited ROS generation during NIR light exposure [16–18]. Moreover, excessive $Cu^{2+}$ released from the nanospheres may damage tissues and therefore, to serve as photosensitizers, CuS nanospheres are usually modified for light-controlled therapy.

Curcumin is a natural herbal medicine with anti-inflammatory, antioxidant, anti-atherosclerosis, anti-tumor and other pharmacological effects [19]. There are abundant delocalized electrons on the surface of curcumin due to the conjugation effect and the electrons can be used

* Corresponding authors at: Shanxi Key Laboratory of Biomedical Metal Materials, College of Materials Science and Engineering, Taiyuan University of Technology, Taiyuan 030024, China (X. Zhang).
*E-mail addresses:* xhyao@tyut.edu.cn (X. Yao), zhangxiangyu@tyut.edu.cn (X. Zhang).

https://doi.org/10.1016/j.cej.2022.139474
Received 28 July 2022; Received in revised form 12 September 2022; Accepted 25 September 2022
Available online 29 September 2022

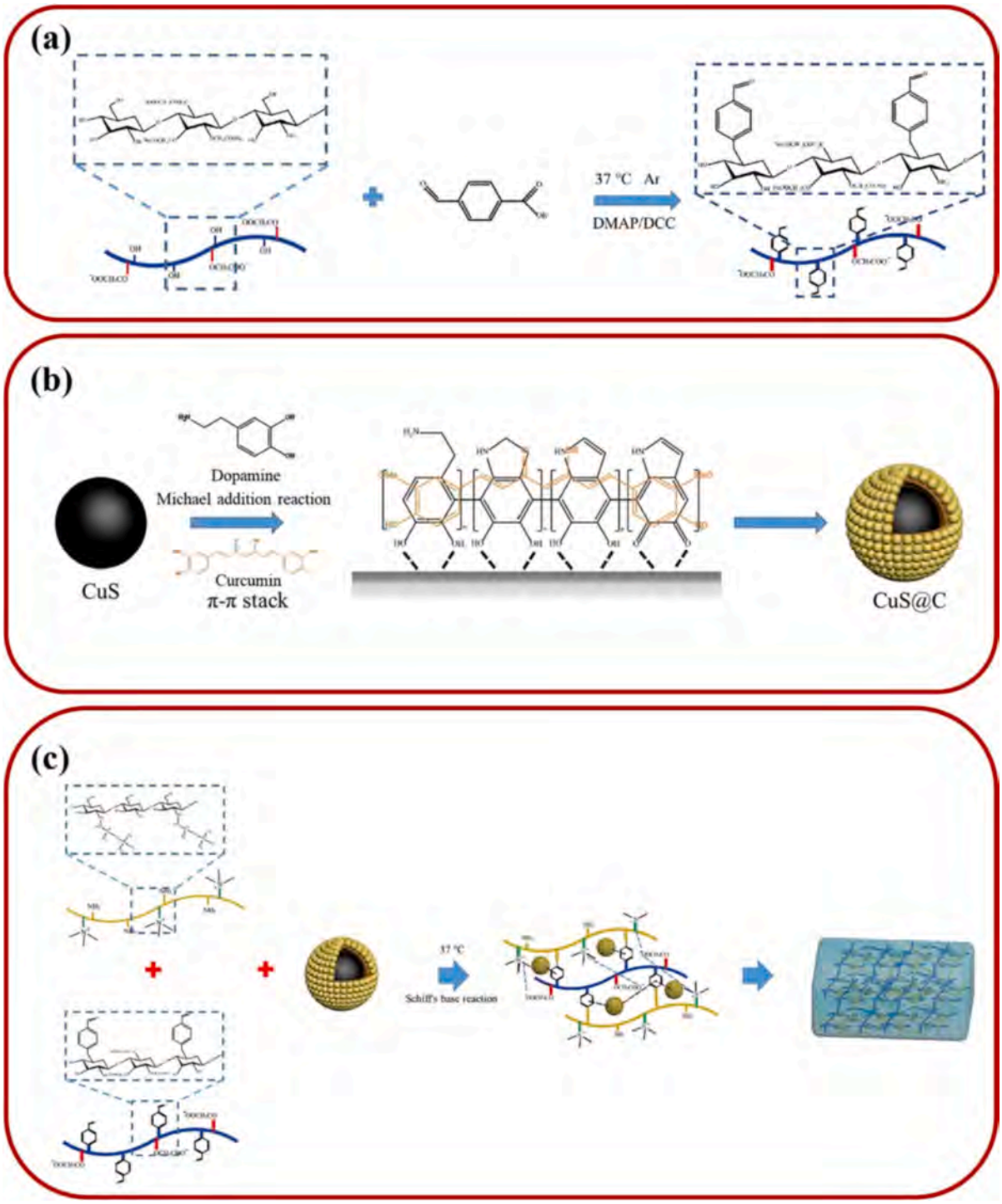


**Scheme 1.** Schematic diagram showing the preparation of (a) CMCBA molecules, (b) CuS@C nanospheres, and (c) CuS@C hydrogel.

as carriers in photocatalytic processes, so that curcumin is an *n*-type semiconductor [20]. Hence, if a hybrid p-n junction is formed between curcumin and CuS, electrons in the *n*-type semiconductor can move to the p-type semiconductor to form an internal electric field that not only promotes rapid separation and migration of photogenerated carriers, but also destroys the conjugated structure of curcumin to enhance the photocatalytic activity.

Chitosan, carboxymethyl cellulose (CMC), and the related derivatives are natural, non-toxic, and biodegradable polysaccharides existing in nature [21–23]. They are potential candidates for the preparation of multifunctional hydrogels. Recently, injectable hydrogels based on dynamic bond cross-linking have attracted much attention for treatment of complex wounds [24,25]. In this work, 4-formylbenzoic acid is grafted onto the side group of CMC by esterification to introduce the benzene ring and aldehyde group to the CMC molecular chain (Scheme 1a). In this way, an injectable and self-healing hydrogel based on the modified CMC molecule (CMCBA) and hydroxypropyl trimethyl ammonium chloride chitosan (HACC) can be formed by the Schiff base reaction and electrostatic interactions [26–28]. The CuS nanospheres are synthesized by a one-step solvothermal process. Curcumin is then decorated on the surface of the CuS nanospheres by introducing polydopamine (PDA) which is known to be strongly adhesive and can be

combined with curcumin by π-π stacking to construct the organic–inorganic hybrid of CuS@C p-n junction (Scheme 1b). The CuS@C nanospheres are then dispersed in the modified CMC solution and the dispersion is co-injected with HACC to obtain the CuS@C hybrid hydrogel (Scheme 1c). The benzene ring introduced to the side group of CMC improves not only the dispersibility, but also adhesiveness of CuS@C in the hydrogel by π-π conjugation between the benzene ring and curcumin [29,30]. Herein, the antibacterial activity and biocompatibility of the multifunctional hybrid hydrogel are evaluated by *in vitro* and *in vivo* assays. The hydrogel possesses injectable and self-healing properties and shows highly effective antibacterial efficacy due to the combined effects of hyperthermia and ROS for accelerated wound healing. Moreover, the organic coating composed of curcumin and PDA reduces release of $Cu^{2+}$ and improves the biocompatibility of the CuS nanospheres.

## 2. Experimental details

### 2.1. Materials

$Cu(NO_3)_2{\cdot}3H_2O$, polyvinylpyrrolidone (PVP), dimethyl sulfoxide (DMSO) and methanol were purchased from Tianjin Damao Chemical Reagent Factory, China and dopamine hydrochloride, curcumin, 3-(4,5-dimethylthiazol-2-yl)-2,5-diphenyltetrazolium bromide (MTT), phosphate buffer (PBS), fetal bovine serum, acridine orange (AO), and propidium iodide (PI) were produced by Shanghai Biotechnology Development Co. ltd. (China). Carboxymethyl cellulose (CMC), 4-dimethylaminopyridine, N, N'-dicyclohexylcarbodiinide, tetrahydrofuran (THF) and hydroxypropyl trimethyl ammonium chloride chitosan (HACC) were purchased from Shanghai Macklin Biochemical Co., ltd. (China). Cellulase, 5,5-dimethyl-1-pyrroline-*n*-oxide (DMPO), (3-Aminopropyl) trimethoxysilane (APTMS), $Na_2SO_4$, glutathione (GSH), *O*-nitropheny-*β*-D-galactopyranoside (ONPG), and glutaraldehyde were obtained from by Shanghai Aladdin Biochemical Technology Co., ltd. (China). The enhanced BCA protein assay kit (P0010) and live-dead cell staining kit were bought from Beyotime Biotechnology Co., ltd. (China). Dulbecco's modified eagle medium (DMEM) was produced by Thermo Fisher Scientific.

### 2.2. Synthesis of CuS nanospheres

The CuS nanospheres were prepared by a solvothermal method. 0.483 g of $Cu(NO_3)_2{\cdot}3H_2O$, 0.4 g of PVP and 0.3 g of thioacetamide were introduced to 30 mL of DMSO and stirred vigorously until a homogenous green solution was formed. The solution was transferred to a Teflon-lined stainless-steel autoclave and maintained at 120 ℃ for 12 h. The obtained CuS powder was collected by centrifugation after rinsing with deionized water and ethanol several times.

### 2.3. Synthesis of CuS@C nanospheres

The CuS nanospheres were dispersed in 100 mL of deionized water to which 100 mg of dopamine hydrochloride and 50 mg of curcumin were added. The mixture was stirred at 25 ℃ for 24 h to form CuS@C nanospheres where then collected by centrifugation and freeze-dried for 12 h.

### 2.4. Synthesis of benzaldehyde-grafted carboxymethyl (CMCBA) cellulose

5 g of CMC and 100 mL of THF were placed in a 500 mL flask. 2.06 g of 4-formylbenzoic acid and 1.7 g of DMAP and DCC were put in the flask and stirred for 24 h under $N_2$. The products were washed with THF and diethyl ether three times. CMCBA cellulose was obtained by centrifugation and dried in a vacuum oven.

### 2.5. Synthesis of hybrid hydrogels

4 g of the CMCBA powder and HACC were dissolved in 100 mL of deionized water, respectively. 0.01 g of curcumin, CuS nanospheres, and CuS@C nanospheres were added, respectively, to 0.5 mL of the CMCBA solution and stirred until homogeneous dispersions were formed. Afterwards, 0.5 mL of the HACC solution were added to the dispersions to prepare the curcumin hydrogel, CuS hydrogel and CuS@C hydrogel, respectively. Meanwhile, 0.5 mL of the HACC solution were added to the pure CMCBA solution to prepare the CMC/HACC hydrogel as a control group.

### 2.6. Materials characterization

Field-emission scanning electron microscopy (FE-SEM, JSM-7001F, JEOL) was performed to observe the morphology of the nanospheres and hydrogels. Field-emission transmission electron microscopy (FE-TEM, JEM-2100F, JEOL) and X-ray diffraction (XRD) were used to analyze the structure of the CuS and CuS@C nanospheres. X-ray photoelectron spectroscopy (XPS, K-alpha, Thermo) was conducted to determine the chemical composition. The JS94 micro electrophoresis apparatus (Powereach, China) was used to determine the zeta potentials and ultraviolet–visible-NIR (UV–vis-NIR) diffuse reflectance absorption spectra were acquired. Ultraviolet photoemission spectroscopy (UPS) was carried out to analyze the band structure and Fourier transform infrared (FTIR) spectroscopy was employed to analyze the surface functional groups. The diameter was recorded by dynamic light scattering (DLS).

### 2.7. Water content

To study the water content, the hydrogels were synthesized and soaked in PBS until they reached water saturation. The mass of the hydrogels in the saturated state was weighed as $W_0$. Then, the hydrogels were placed in a lyophilizer and freeze-dried to an absolutely dry state. The mass of the hydrogels in the absolutely dry state was weighed as $W_t$. Results were calculated as water content with the equation: $S = (W_0\text{-}W_t)/W_0$.

### 2.8. Viscosity test

The viscosity of hydrogels was tested by a rotational rheometer (ARES-G2). The viscosity was measured with the variation of the frequency increased from 1 to 100 $rad{\cdot}s^{-1}$. The temperature was 37 ℃. The strain of hydrogel was 10 %.

### 2.9. Self-healing ability of hybrid hydrogels

The self-healing experiment was carried out by macroscopic method and rheological property measurements. Pure CMC/HACC, curcumin, CuS, and CuS@C hydrogels were cut into pieces and put together with another piece of CMC/HACC hydrogel, respectively. The self-healing process was monitored by a camera.

The rheological property of CuS@C hydrogels was investigated by a rotational rheometer (ARES-G2) to quantitatively evaluate the self-healing ability of the hydrogels. First, dynamic frequency sweep rheological test was performed on the intact CuS@C hydrogel. After the test, the CuS@C hydrogel was divided into two pieces and put back into the fixture. After 20 min, 25 min and 30 min in the fixture, dynamic frequency sweep rheological tests were performed again. Finally, the self-healing ability of CuS@C hydrogels was quantitatively measured according to the changes in the rheological property of the hydrogels.

### 2.10. Injectable ability of hybrid hydrogels

The curcumin, CuS, and CuS@C nanospheres were dispersed in the

CMCBA solution and the dispersions were blended with HACC to form the premix that was transferred to a 20 mL syringe. The injection process and the morphology of the injected hydrogel were recorded by a camera.

### 2.11. Degradability of CuS@C hydrogel

To evaluate the degradability of the CuS@C hydrogel, the freeze-dried hydrogel was immersed in 1 mL of PBS containing 0.1 % cellulase at a constant temperature (37 ℃). The remaining weight of the hydrogel was recorded every 5 min. The remaining weight % of the hydrogels is defined by the following equation:

$$\text{Weight remaining ratio of hydrogel } (\%) = W_t/W_0 \times 100\ \%,$$

where $W_t$ and $W_0$ are the dry weights of the remaining hydrogel after degradation at different time points and the dry weight of the initial hydrogel, respectively.

### 2.12. Photodynamic and photothermal properties

The electron paramagnetic resonance (EPR) spectra were acquired on an electron spin resonance spectrometer (EMXPLUS10/12, Bruker, Germany) to evaluate the photodynamic properties. DMPO was prepared in an 80 mM solution with deionized water and methanol as solvents. The superoxide radicals ($\bullet O_2^-$) were selectively absorbed by the DMPO methanol solution, whereas the DMPO water solution was a selective absorbent for hydroxyl radicals (•OH). 0.01 g of curcumin, CuS, and CuS@C were added to 1 mL of the DMPO solution (aqueous solution and methanol solution), respectively. After irradiation with 808 nm NIR light for 10 min, the DMPO solution was transferred to EMXPLUS10/12 to detect ROS.

The photothermal effects of the hydrogels were monitored by FLIR infrared thermal imaging. 1 mL of the PBS solution was added to the hydrogel and irradiated with 808 nm NIR light for 10 min. The temperature of the hydrogel was recoreded at 1 min intervals. To investigate the cyclic heating capacity of the CuS@C hydrogel, four heating–cooling cycles were implemented and the temperature was recorded by the FLIR infrared thermal imager every 2 min.

### 2.13. Electrochemical measurements

The CuS and CuS@C nanospheres served as the photo-anodes to monitor the transient photocurrent response and electrochemical impedance spectroscopy (EIS) was performed to investigate the improved catalytic activity of CuS@C nanospheres. The experiments were performed on an electrochemical workstation (CHI660E, China) with the conventional three-electrode system, in which the sample, Ag/AgCl electrode, and platinum foil were the working, reference, and counter electrodes, respectively. To prepare the working electrode, indium tin oxides (ITO) was immersed in APTMS for 3 h and washed with 2.5 % glutaraldehyde. 4 mg of the sample were dispersed in 1 mL of deionized water and then 200 μL of the solution was placed on a piece of conductive ITO glass to form the working electrode. The electrochemical measurements were performed in 0.1 M $Na_2SO_4$ at 25 °C. The photocurrents were measured during 808 nm NIR light irradiation and EIS was conducted at the open circuit potential in the frequency range between 100 kHz and 0.01 Hz together with a sinusoidal potential of 10 mV under 808 nm NIR light irradiation.

### 2.14. Theoretical calculation

To illustrate the charge transfer process between curcumin and CuS nanospheres, DFT calculation was performed. The spin theoretical simulation was carried out using the Vienna Ab-initio Simulation Package (VASP) version 6.1.2 with the generalized gradient approximation (GGA) and Perdew-Burke-Ernzerhof (PBE) exchange and correlation functionals. The dynamic cut-off energy of the plane-wave basis function was set to 400 eV and Monkhorst-Pack meshes with a size of 2 × 3 × 1 were used to sample the bulk Brillouin zone. The microstructure of the CuS@C nanospheres was built based on a 3 × 2 × 1 supercell. The four layers of atoms on the bottom of the CuS nanospheres were fixed as the bulk part, whereas the other atoms (surface atoms of CuS nanospheres, PDA molecules, and curcumin molecules) were allowed to relax below 0.02 eV $Å^{-1}$. The hybrid Heyd-Scuseria-Ernzerhof (HSE06) method was utilized to determine the exact band structures of the CuS@C nanospheres.

### 2.15. Glutathione experiments

Glutathione (GSH) plays an important role in maintaining the membrane structure and preventing membrane oxidation. Decreases of the GSH concentration were assessed using Ellman's experiments [31,32]. The $1 \times 10^{-3}$ M GSH bicarbonate buffer solution was added to the surface of the hydrogel and irradiated with 808 nm NIR light for 10 min. The irradiated GSH solution on the hydrogel was extracted and mixed with 2.4 mL of 0.05 M Tris-HCl (pH = 8) and 45 μL of $100 \times 10^{-3}$ M 5, 5′-dithiobis (2-nitrobenzoic acid) (Ellman's reagent). The $1 \times 10^{-3}$ M GSH solution was the negative control. Degradation of GSH was evaluated by measuring the absorbance of the solution at 410 nm by spectrophotometry.

### 2.16. In vitro antibacterial properties

The antibacterial activities of the hybrid hydrogels against *Staphylococcus aureus* (*S. aureus*, ATCC 25923) and *Escherichia coli* (*E. coli*, ATCC 10536) were evaluated by the spread plate method. The CMC/HACC hydrogel without light irradiation was the control group. The hydrogels were placed on a 24-well plate and 1 mL of the bacterial suspension ($1 \times 10^5$ CFU/mL) was placed on the hydrogel surface. The hydrogels were exposed to 808 nm NIR light (0.6 W/$cm^2$) for 10 min and the temperature of the hydrogels was controlled below 50 ℃ during irradiation. The irradiated bacterial suspension was diluted 100 times and 100 μL of the diluted suspension were spread on a standard agar medium. The agar plates were cultured for 24 h at 37 ℃. The CFU number was counted and the antibacterial efficiency was calculated by the following equation:

$$\text{Antibacterial efficiency } (\%) = \frac{\text{CFUControl-CFUSample}}{\text{CFUControl}},$$

where $CFU_{Control}$ is the number of CFU corresponding to the CMC/HACC hydrogel without 808 nm NIR light irradiation. Furthermore, in order to determine the optimum content of CuS@C nanospheres, hydrogels with different CuS@C contents (0.005 g, 0.01 g and 0.02 g) were prepared and tested for the above-mentioned antibacterial property.

The irradiated *E. coli* and *S. aureus* suspensions were fixed with 2.5 % glutaraldehyde for 40 min and dehydrated using graded ethanol solutions (20, 40, 60, 80, 90 and 100 %) for 15 min. The morphology of the bacteria was observed by SEM. A Live/Dead kit (AO/PI) was used to evaluate the anti-biofilm activity of the hydrogels. 1 mL of the *S. aureus* solution ($10^8$ CFU/mL) was dropped onto the surface of a cell climbing slice and cultured for 48 h. The hydrogels were then placed on the surface of cell climbing slice and after exposure to 808 nm NIR light for 10 min, the slice was stained in darkness for 15 min and then examined under a confocal laser scanning microscope (CLSM).

Considering that a high temperature may damage skin tissues near the wound, the antibacterial properties of the hydrogels were determined at a relatively low temperature (45 ℃). 1 mL of the bacterial solution was dropped onto the surface of the hydrogels and exposed to 808 nm NIR light for 10 min. The surface temperature of the hydrogels was controlled to be below 45 ℃ by cooling during irradiation.

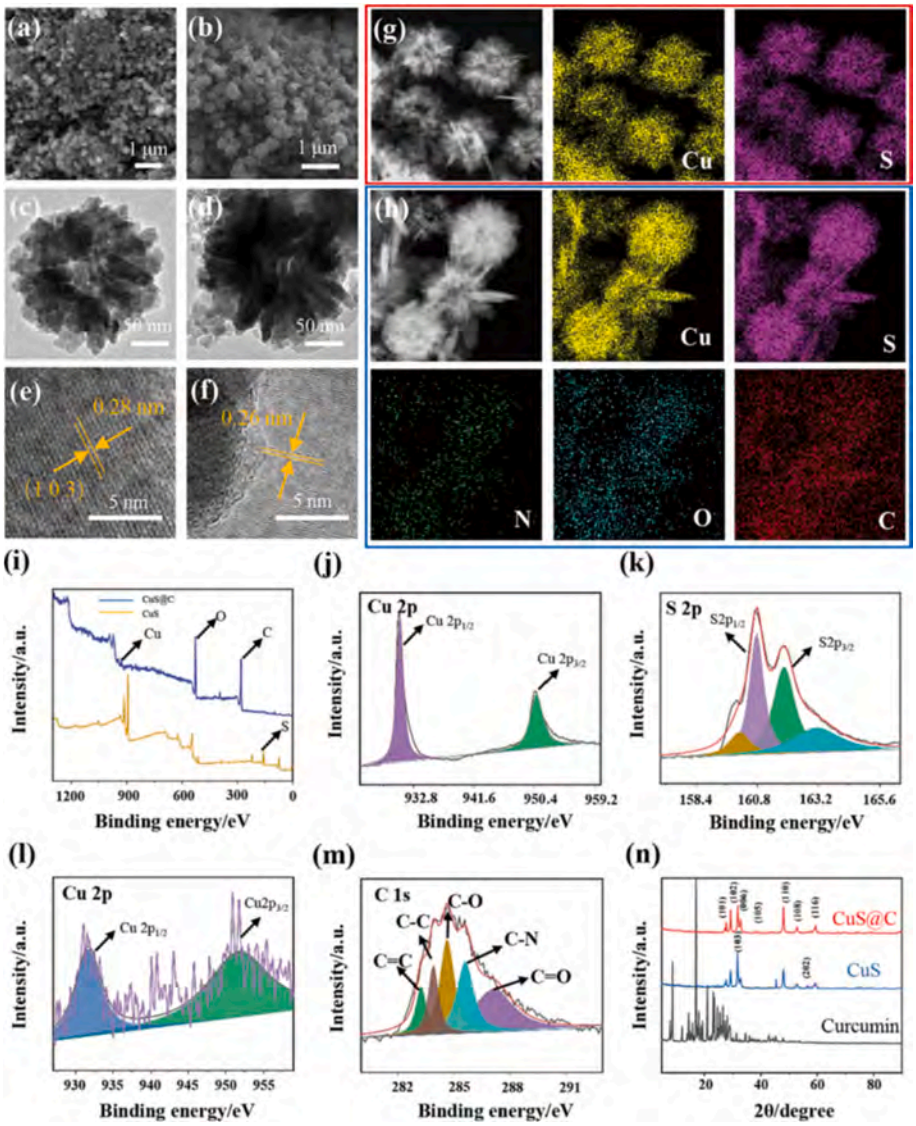


**Fig. 1.** SEM images of (a) CuS nanospheres and (b) CuS@C nanospheres; TEM images of (c) CuS nanospheres and (d) CuS@C nanospheres; HR-TEM images of (e) CuS nanospheres and (f) CuS@C nanospheres; EDS elemental maps of (g) CuS nanospheres and (h) CuS@C nanospheres; (i) XPS survey spectra; High-resolution XPS spectra of (j) Cu 2p and (k) S 2p of the CuS nanospheres; High-resolution XPS spectra of (l) Cu 2p and (m) C 1 s of the CuS@C nanospheres; (n) XRD patterns.

### 2.17. Bacterial membrane permeability

*O*-nitropheny-*β*-D-galactopyranoside (ONPG) was used to study the membrane permeability of the bacteria. 1 mL of the *S. aureus* and *E. coli* solution ($1 \times 10^8$ CFU/mL) was added to the surface of hydrogels and 808 nm NIR light illumination proceeded for 10 min. Afterwards, the bacterial solution was transferred to a 24-well plate and 500 μL of the ONPG solution (0.75 M) were added. The OD value of the yellow supernatant was determined on a microplate reader at 420 nm.

### 2.18. Protein leakage

1 mL of the *S. aureus* and *E. coli* solution ($1 \times 10^8$ CFU/mL) was placed on the surface of hydrogels and irradiated with 808 nm NIR light for 10 min. The supernatant was extracted and centrifuged at 5,000 rpm for 12 min. The BCA Protein Assay Kit (P0010) was used to study the leached proteins in the bacteria solution.

### 2.19. Anti-biofilm assay

The anti-biofilm activity was evaluated by the crystal violet staining method. 1 mL of *S. aureus* and *E. coli* solution ($1 \times 10^8$ CFU/mL) was injected into a 24-well plate and cultured at 37° C for 36 h. After incubation, CMC/HACCl, curcumin, CuS and CuS@C hydrogel were added to 24-well plates, respectively, and irradiated with 808 nm NIR laser for 10 min. Subsequently, the hydrogels were removed from bacterial solution and washed three times with PBS to remove floating bacteria. After irradiation, 100 μL methanol was added to the 24-well plate and aspirated after 15 min of incubation. 100 μL of 1 % crystal violet staining solution was added to each well and stained for 5 min at room temperature (25 ℃). After that, the staining solution was aspirated and washed three time with DI to remove excess staining solution. 100 μL of 33 % acetic acid solution was added to each well and incubated for 30 min to dissolve the stained bacteria. At a wavelength of 570 nm, the OD value of lysate was measured by microplate reader (Infinite F50, TECAN). Three specimens each group were tested.

### 2.20. In vitro biocompatibility assessment

#### 2.20.1. Cell culture

The fibroblasts (*NIH-3 T3*) and endothelial cells (*EA. Hy 926*) were cultured in Dulbecco's modified eagle medium (DMEM) supplemented

with 10 % FBS, 1 % penicillin, and streptomycin at 37 °C in 5 % $CO_2$ and 95 % air.

#### 2.20.2. Cell viability assay

The Live/Dead viability kit was used to evaluate the cell viability of the hydrogels. The hydrogels were immersed in 1 mL of the medium for 24 h. The leaching solution was transferred to the cell crawls and co-cultured with fibroblasts and endothelial cells ($2 \times 10^4$ cells/cm$^2$) for 1, 3 and 5 days, respectively. Afterwards, the medium was removed and 1 mL of the Live/Dead staining reagent was added to the cell crawls for 40 min in darkness. The staining reagent was washed with PBS and the image was collected by CLSM.

#### 2.20.3. MTT assay

The 3-(4,5-dimethylthiazol-2-yl)-2,5-diphenyltetrazolium bromide (MTT) assay was used to evaluate the cell viability quantitatively. 1 mL of the leaching solution was co-cultured with 1 mL of the cell solution ($2 \times 10^4$ cells/cm$^2$) on the surface of the cell crawls for 1, 3 and 5 days. The solution containing 100 μL of MTT (5 mg/mL) and 900 μL of the medium was added to the cell crawls and incubated for 4 h in darkness. Afterwards, the MTT solution was removed and 1 mL of DMSO was applied to dissolve the crystals. The OD values of the crystal solution were determined on a microplate reader at 490 nm.

### 2.21. Animal experiments

The animal programs followed the "Taiyuan University of Technology" guidelines for the care and use of laboratory animals and were approved by the Animal Ethics Committee of the "International Standards for Animal Welfare" (Approval No.TYUT-202105001). The rats (SD rats, 280–350 g, body weight) were purchased from Shanxi Medical University. The mice were divided into five groups and a square wound was cut on the back of each mouse after anesthesia. 50 μL of the *S. aureus* solution ($1 \times 10^8$ CFU/mL) were introduced to the wounds to establish the infection model (Fig. 9a). The 3 M wound dressing, CMC/HACC, curcumin, CuS, and CuS@C hydrogels were applied to the wounds and then irradiated with 808 nm NIR light for 10 min. During irradiation process, the temperature of the wound was controlled to be below 45 ℃ with the aid of an FLIR infrared thermal imager that recorded the temperature of the hydrogels in real time. After feeding for 2 days, half of the mice were sacrificed for hematoxylin and eosin (H&E) and Giemsa staining. The remaining ones were cultured and the wounds were recorded every 2 days. To determine the antibacterial effects on the wounds, the same light was applied to the wounded area on day 2 and day 4. Meanwhile, the ichor on the surface of the wound was extracted and transferred to an agar plate for cultivation for 24 h. After 10 days, all the mice were sacrificed and the tissues around the wounds were stained with H&E, Giemsa, and Sirius red stain. The major organs were also removed and stained with H&E to verify the *in vivo* biosafety.

### 2.22. Statistical analysis

All the experiments were conducted in triplicate and the experimental data were evaluated as mean ± standard deviation based on the SPSS 14.0 software. The one-way ANOVA combined with a Student–Newman–Keuls (SNK) post hoc test was applied to determine the level of significance. In the statistical evaluation, $p < 0.05$, $p < 0.01$, and $p < 0.001$ were regarded as significant, highly significant, and extremely significant, respectively.

## 3. Results and discussion

### 3.1. Characterization of CuS@C nanospheres

The CuS@C nanospheres are synthesized by a two-step method. The CuS nanospheres are prepared by a solvothermal method and dried for ensuing modification. Dopamine is used as a cross-linking agent to graft curcumin onto the surface of CuS nanospheres in an aqueous solvent. Dopamine spontaneously transforms into PDA by polymerization in the Michael addition reaction under aerobic conditions and curcumin molecules are immobilized on the surface of the CuS nanospheres during polymerization with π-π conjugation. The zeta potentials of CuS, PDA, and curcumin are −1.41, −24.2, and 1.32 eV (Fig. S1a), respectively, indicating that curcumin can be assembled on the surface of the nanospheres by electrostatic adsorption. The SEM image of CuS in Fig. 1a shows nanospheres with diameters of 150–200 nm and after modification with curcumin, the mean diameter of the CuS@C nanospheres increases slightly (Fig. 1b). DLS test indicates that the particle size of CuS@C nanospheres mainly distributed between 250 and 500 nm, which is consistent with the results of SEM image (Fig. S2). The TEM images (Fig. 1c and 1d) reveal that the nanospheres are assembled from nanoflakes. A lattice spacing of 0.28 nm corresponding to the (1 0 3) plane of CuS is observed from the high-resolution transmission electron microscopy (HR-TEM) image of CuS (Fig. 1e). The lattice spacing of 0.26 nm in the outermost shell of CuS@C nanospheres can be attributed to the curcumin crystal (Fig. 1f). The elemental maps in Fig. 1g reveal that Cu and S are uniformly distributed in CuS and Fig. 1h indicates even distributions of Cu, S, N, C, and O in CuS@C.

The chemical states of CuS and CuS@C are determined by XPS. As shown in the survey spectra (Fig. 1i), the intensity of the C and O peaks from CuS@C is significantly higher than that from CuS, confirming that CuS is modified with PDA and curcumin. The high-resolution spectra of Cu and S of CuS are shown in Fig. 1j and 1 k. The binding energies of S $2p_{3/2}$, S $2p_{1/2}$, Cu $2p_{3/2}$ and Cu $2p_{1/2}$ are 162.8, 161.8, 951.5 and 931.7 eV, respectively, illustrating the presence of CuS in the CuS nanospheres. In the high-resolution C 1 s spectrum of CuS@C, the peak of C—N at 285.6 eV demonstrates existence of PDA and the peaks of C═C and C═O appear at 283.2 and 287.2 eV, respectively, indicate that curcumin is immobilized on the surface of CuS (Fig. 1m) [33,34]. The FTIR spectra of curcumin, CuS, and CuS@C are displayed in Fig. S1b. The representative peaks of curcumin powder at 1506, 1605, 1279, and 1152 cm$^{-1}$ are assigned to C═O, C═C and C—O stretching vibrations, respectively. The characteristic peaks of C observed from CuS@C confirm the combination of curcumin and CuS. The XRD patterns of curcumin, CuS and CuS@C are presented in Fig. 1n. The characteristic peaks of CuS can be indexed to the standard pattern (JCPDS No. 06–0464), which is also observed from CuS@C. No C peaks are observed from the hybrid nanospheres because of the small concentration. These results corroborate that grafting of PDA and curcumin do not alter the phase structure of CuS.

### 3.2. Fabrication and characterization of CuS@C hydrogel

The preparation process of CuS@C hydrogel is illustrated in scheme 1. CMCBA is synthesized by a one-step nucleophilic addition reaction. Under the catalytic conditions of 4-dimethylaminopyridine/N, N'-dicyclohexylcarbodiimide, α-hydroxy (α-OH) on the side chain of the CMC molecule reacts with the carboxyl group (COOH) on 4-formylbenzoic acid to form an ester bond. The water-soluble HACC is utilized as an amino donor to alleviate the problem of the limited solubility of chitosan in the neutral medium. The quaternary ammonium group on the side chain of quaternary ammonium salt chitosan not only increases the solubility of the molecule in a neutral solution, but also generates electrostatic adsorption with the carboxyl group on the CMCBA molecule. Finally, the three components of CMCBA, HACC, and CuS@C nanospheres are mixed mechanically room temperature. The π-π stacking is formed between the benzene ring on both curcumin and PDA molecule and on the side chain of CMCBA. The carboxyl group on the CMCBA adsorbs the quaternary ammonium group on the HACC electrostatically and meanwhile, the aldehyde groups on CMCBA can be cross-linked with the amino groups on HACC by the Schiff base reaction to form a polymer network. Under the action of these three dynamic

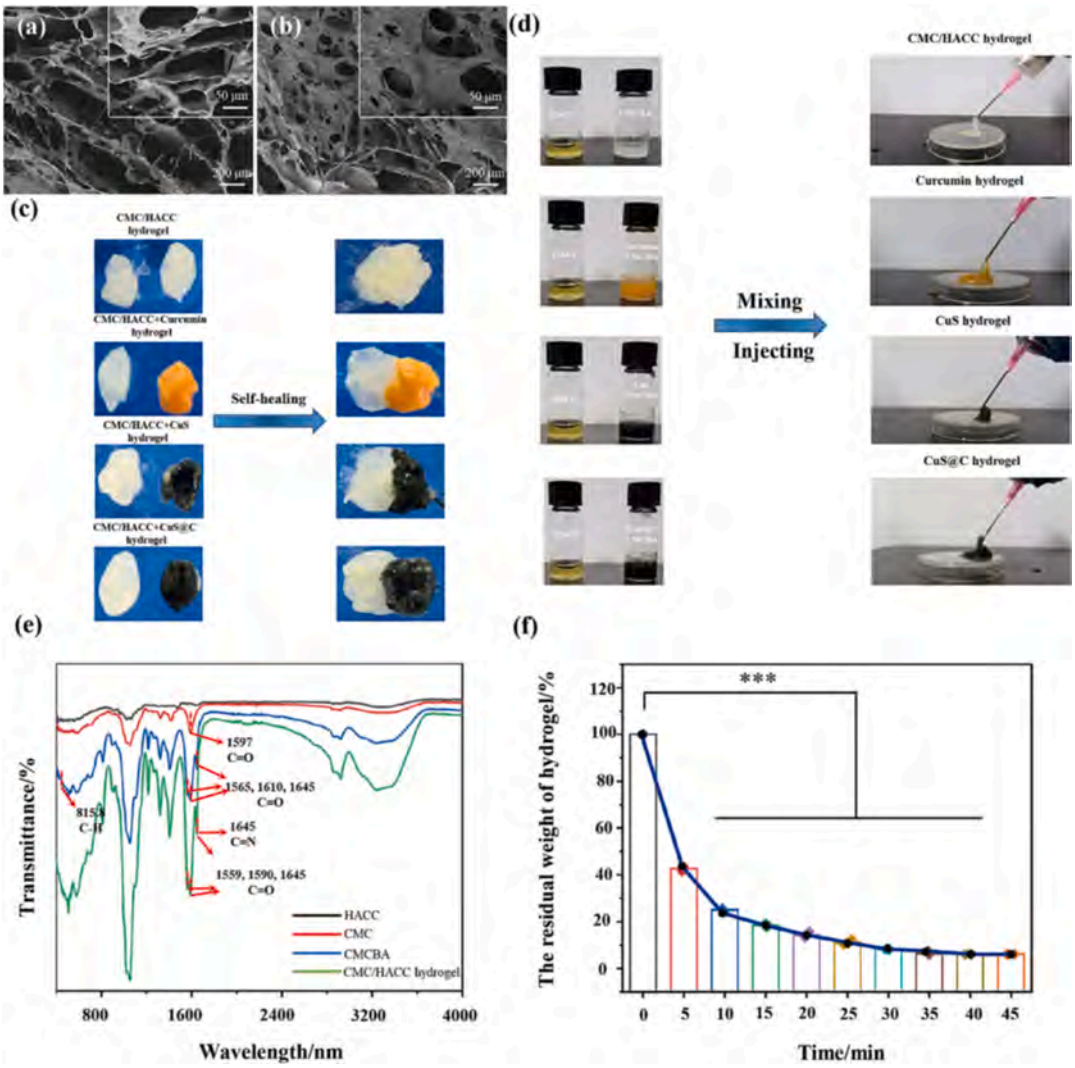


**Fig. 2.** SEM images of (a) CMC/HACC hydrogel and (b) CuS@C hydrogel; (c) Illustration of the self-healing ability of the hydrogels; (d) Photograph of the injecting process of the hydrogels; (e) FT-IR spectra of HACC molecules, CMC molecules, CMCBA molecules and CMC/HACC hydrogels; (f) Degradation of the CMC/HACC hydrogel in the 0.1 % cellulase solution at 37 ℃. (***$p < 0.001$).

bonds, a degradable and self-healing light-controlled antibacterial hydrogel containing CuS@C nanospheres is based on CMCBA and HACC is prepared. The microstructure of the CMC/HACC and CuS@C hydrogels observed by SEM (Fig. 2a and 2b) shows that the hydrogels have a porous structure and the CuS@C nanospheres appear on the surface of the CuS@C hydrogel.

The hydrogels prepared based on dynamic bond cross-linking generally possess excellent self-healing and injectable properties [35]. When the hydrogels are damaged to a certain range, the molecules on the section will re-form dynamic bonds at room temperature. The self-healing property and injectability of the hybrid hydrogels are evaluated. As shown in Fig. 2c, the CMC/HACC hydrogel looks white. After introducing curcumin, the color of the hydrogel changes from white to yellow, whereas both the CuS and CuS@C hydrogels are black. When the CMC/HACC hydrogel is put together with CMC/HACC, curcumin, CuS, and CuS@C hydrogels, respectively, the two hydrogels fuse into one. The results indicate that the CMC/HACC hydrogel has good self-healing ability and the incorporation of curcumin, CuS, or CuS@C has no effect on the self-healing property. Furthermore, the rheological property is monitored in real-time using a rotational rheometer to quantitatively evaluate the self-healing ability of CuS@C hydrogel (Fig. S3). After reattached and placed in the fixture for 20 min, the hydrogel gradually recovered and returned to the pre-cutting level at 30 min. The results toughly demonstrate the self-healing ability of CuS@C hydrogel.

The gelation process of the hybrid hydrogels is shown in Fig. 2d. The pure CMCBA solution and curcumin, CuS and CuS@C – containing CMCBA dispersions have excellent flowability as well as the HACC solution. However, when the CMCBA solution or dispersion are transferred to a syringe, they become solid hydrogels and the extrusion experiments prove the injectability of the hydrogels.

The FTIR spectra of HACC, CMC and CMCBA molecules as well as CMC/HACC hydrogel are presented in Fig. 2e. The characteristic absorption peak of CMC molecules at 1597 cm-1 can be assigned to C═O stretching of the carboxymethyl bond. However, the absorption peak of CMCBA around 1610 $cm^{-1}$ is split into three peaks at 1565, 1610 and 1645 $cm^{-1}$ attributable to C═O stretching of the aromatic ester, carboxymethyl bond, and aromatic aldehyde, respectively. Compared to CMC and CMCBA molecules, a characteristic absorption peak appears around 815.8 cm-1 from both the HACC molecule and CMC/HACC hydrogel due to C—H bending of the benzene ring. The results verify that 4-formylbenzoic acid is grafted onto the CMC molecule. With regard to CMC/HACC hydrogel, the absorption peaks at 1559 and 1590 $cm^{-1}$ correspond to C═O stretching of the aromatic ester and carboxymethyl bond, respectively, and the peak at 1645 $cm^{-1}$ arises from the Schiff base group [36]. The CMCBA and HACC molecules have opposite charges (Fig. S4) thus producing electrostatic adsorption between the CMCBA

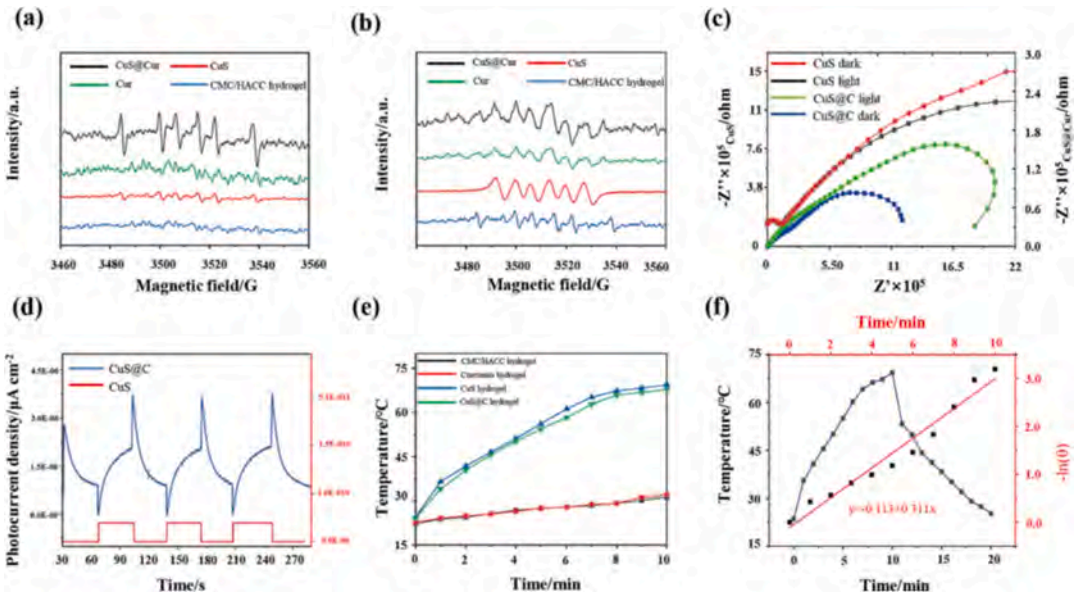


**Fig. 3.** EPR spectra of (a) RO• and (b) $^{\bullet}O_2^-$ of curcumin, CuS and CuS@C; (c) Nyquist plots of CuS and CuS@C with or without light irradiation; (d) Transient photocurrent densities of CuS and CuS@C under NIR light irradiation; (e) Photothermal curves of different hydrogels under 808 nm laser; (f) Photothermal-conversion efficiency (η) of the CuS@C hydrogel under 808 nm laser irradiation. (***$p < 0.001$).

and HACC molecules.

The β-1, 4 glycosidic bond in the CMC molecule can be destroyed by cellulase and hence, the three-dimensional network structure of the HACC/CMC hydrogel can be broken in the cellulose solution resulting in degradation of the hydrogel. The degradability of CMC/HACC hydrogel is shown in Fig. 2f. In the first 5 min, the mass of the hydrogel quickly drops to 51 % of the original value because the non-crosslinked part of the hydrogel is decomposed by cellulase. Consequently, the hydrogel shows a nearly linear degradation profile. After degradation for 20 min, the remaining mass of the hydrogel is only 10.4 % of the original one confirming the excellent degradability.

The water content of hydrogels is shown in Fig. S5 (a). The results show that the water content of the hydrogels is 80–82 %, and there is no obvious difference among various hydrogels. The viscosity of hydrogels in Fig. S5 (b) demonstrates that the viscosity of the hydrogels is 2600–2700 Pa·s at low frequency, and there is also no obvious difference among various hydrogels. With the increase of shear frequency, the hydrogels show obvious shear thinning phenomenon, and the viscosity dropped rapidly to 100–170 Pa·s.

### 3.3. Photocatalytic and photothermal properties

To investigate the role of curcumin in the photocatalytic effects of CuS@C, production of ROS by CuS, curcumin, and CuS@C nanospheres is monitored upon 808 nm laser irradiation. As shown in Fig. 3a, after irradiation for 10 min, the yield of •OH produced by the CuS@C nanospheres is significantly higher than that of that produced by the CuS nanospheres, curcumin nanoparticles and CMC/HACC hydrogel. The EPR waveform of CuS@C nanospheres is consistent with the standard waveform of alkoxy radicals (RO•) [37]. RO• is produced by breaking the C—O bond between alkoxy and benzene ring of the curcumin molecule. Fig. 3b shows the $^{\bullet}O_2^-$ signals from CMC/HACC hydrogel, curcumin, CuS, and CuS@C nanospheres. Unlike the results of •OH, the amount of $^{\bullet}O_2^-$ generated by the CuS@C nanospheres is close to that of produced by the CuS nanospheres.

EIS is performed and the photocurrent density is used to evaluate the charge transfer ability, photoelectron generations and hole separation efficiency of CuS@C. As shown in Fig. 3c, the impedance of CuS@C is smaller than that of CuS and compared to CuS, irradiation with the 808 nm laser reduces the impedance of the CuS@C nanospheres more effectively. The lower the impedance, the higher is the charge carrier separation or transformation efficiency. The photocurrent densities of the CuS and CuS@C nanospheres are shown in Fig. 3d. The photocurrents of CuS@C are significantly larger than those of CuS, indicating better transfer and separation of photo-induced electrons at the interface of CuS@C.

CuS nanospheres exhibit strong NIR absorbance due to localized surface plasmon resonance (LSPR) [42]. The photothermal conversion ability of the CuS and CuS@C hydrogels is shown in Fig. 3e. After 808 NIR light (0.6 W $cm^{-2}$) irradiation for 10 min, the temperature rise of CMC/HACC and curcumin hydrogel is only 5–8 °C, but that of CuS hydrogel reaches 44.9 °C (Fig. S6a). After combining with curcumin, the heating curve of the CuS@C hydrogel is basically consistent with that of the CuS hydrogel, indicating that combination of curcumin and CuS does not influence the photothermal conversion ability of CuS. The reproducible heating/cooling curves (Fig. S6b) show that the temperature of the CuS@C hydrogel exhibits a stable on–off effect suggesting good photothermal stability.

The photothermal conversion efficiency (η) of the CuS@C hydrogel is calculated by the following formula: Photothermal conversion efficiency (η) = $hS(T_{max}\text{-}T_0)\text{-}Q_0/W(1\text{–}10^{-A})$, where $T_{max}$ and $T_0$ are the highest temperature and ambient temperature, respectively, $Q_0$ is the absorption energy of the solvent, W is the irradiation power of the light source, and A is the light absorption intensity at 808 nm of the CuS@C hydrogel. The parameter $hS$ is calculated by the following formula: $hS = (m_{H2O}\text{-}C_{H2O})/\tau s$, where $m_{H2O}$ represents the total mass of the solvent ($H_2O$) and τs is the time of the constant quantity of the CuS@C hydrogel. In the cooling period, the following formula is used: $t = -\tau s\ln\theta = -\tau s\ln(T\text{-}T_0)/(Tmax\text{-}T_0)$, in which T represents the real-time temperature. Hence, τs can be estimated from the linear regression curve in the cooling phase. As shown in Fig. 3f, the photothermal conversion efficiency of the CuS@C hydrogel reaches 45.8 % confirming the effectiveness in conversion to thermal energy.

Fig. S7a-c depict the UV–vis-NIR diffuse reflectance absorption spectra of curcumin, CuS and CuS@C nanospheres. Curcumin exhibits strong absorption in the ultraviolet (10–380 nm) and visible ranges (380–780 nm), but no absorption can be observed from the NIR range (>780 nm). The CuS nanospheres exhibit a stronger absorption ability in the full spectrum, especially at 808 nm with a sharp absorption peak. Although absorption by CuS/C is lower than that by the CuS

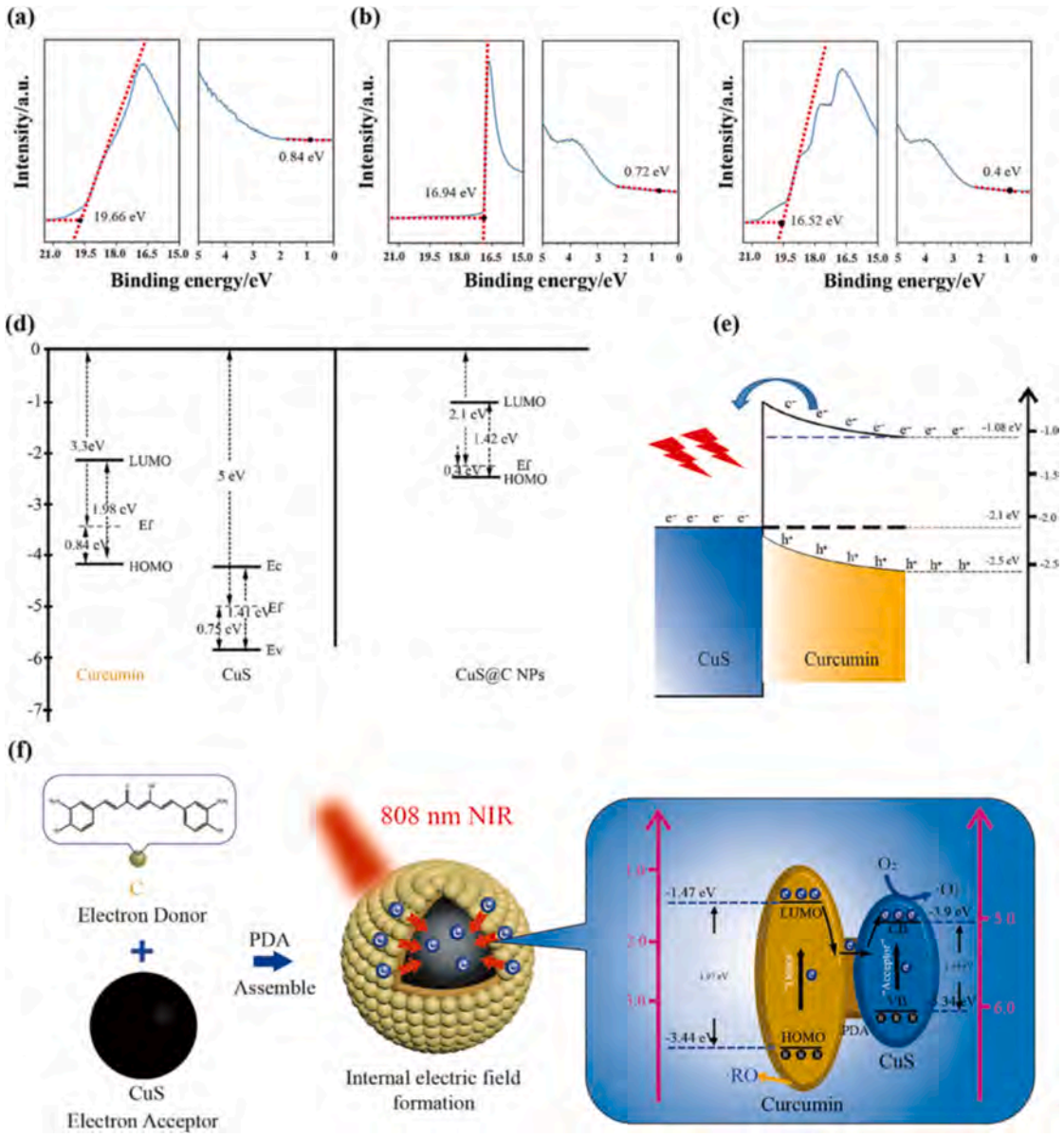


**Fig. 4.** E-cutoff and VB of (a) Curcumin, (b) CuS nanospheres and (c) CuS@C nanospheres; (d) Energy scheme before and after contact between curcumin and CuS; (e) Mechanism for the enhanced yield of ROS *via* NIR-induced progress based on the p-n heterostructure of CuS@C; (f) Charge transfers mechanism of the CuS@C nanospheres upon irradiation with 808 nm light.

nanospheres, CuS/C shows better absorption in the range of 400–900 nm. The bandgaps of curcumin, CuS and CuS@C are calculated by the following equation: $(\alpha hv)^{1/2} = A\ (hv - E_g)$, where $E_g$ is the bandgap of the semiconductor, hv is the photon energy, α is the absorption coefficient, and A is a constant [38]. The Tauc plots are shown in Fig. S5d-f. The bandgaps of curcumin and CuS nanospheres are calculated to be 1.98 eV and 1.41 eV, respectively and after modification with curcumin, the bandgap of the CuS@C nanospheres is 1.42 eV.

UPS is used to analyze the band structure of curcumin, CuS and CuS@C nanospheres. As shown in Fig. 4a-c, the secondary electron cutoff edges (E-cutoff) of curcumin and CuS are 19.66 eV and 16.94 eV, respectively and the corresponding work functions (WF) of curcumin and CuS are calculated to be 3.44 eV and 5.31 eV, respectively, by subtracting the excitation energy of He I (21.22 eV). After modification with curcumin, the E-cutoff of CuS@C nanospheres is 19.52 eV and the corresponding WF of CuS@C is 2.1 eV. The bandgaps between the valence band (VB) and Fermi level (E-fermi) of curcumin, CuS and CuS@C obtained from the Fermi edge shown by the UPS spectra (Fig. 4a-c) are 0.84, 0.72 and 0.4 eV, respectively. The schematic diagram of energy transfer is presented by combining the UPS spectra with UV–vis-NIR diffuse reflectance absorption spectra (Fig. 4d, f). The VB and conduction band (CB) of CuS are measured to be −6.34 eV and −5.32 eV (*vs* vacuum), respectively, and the highest occupied molecular orbital (HOMO) and lowest unoccupied molecular orbital (LUMO) of curcumin are −5.32 eV and −4.14 eV (*vs* vacuum), respectively. The LUMO of the CuS@C nanospheres is −1.08 eV and the HOMO of the CuS@C nanospheres is −2.5 eV. Owing to the difference in the WFs between curcumin and CuS, the WF equilibrium will be achieved by spontaneous electron transfer from curcumin to CuS (Fig. 4e). In this study, the loss of electrons of the curcumin molecule and destruction of the conjugate structure break the connection between the alkoxy group and benzene ring of the curcumin molecule. Therefore, the CuS@C nanospheres generate RO• during 808 nm laser irradiation. The partial electrons transferred from curcumin can form an electron-rich layer on the surface of CuS to reduce $O_2$ into $\bullet O_2^-$. The reduced interface impedance is conducive to the transition of light-excited charge and reduction of

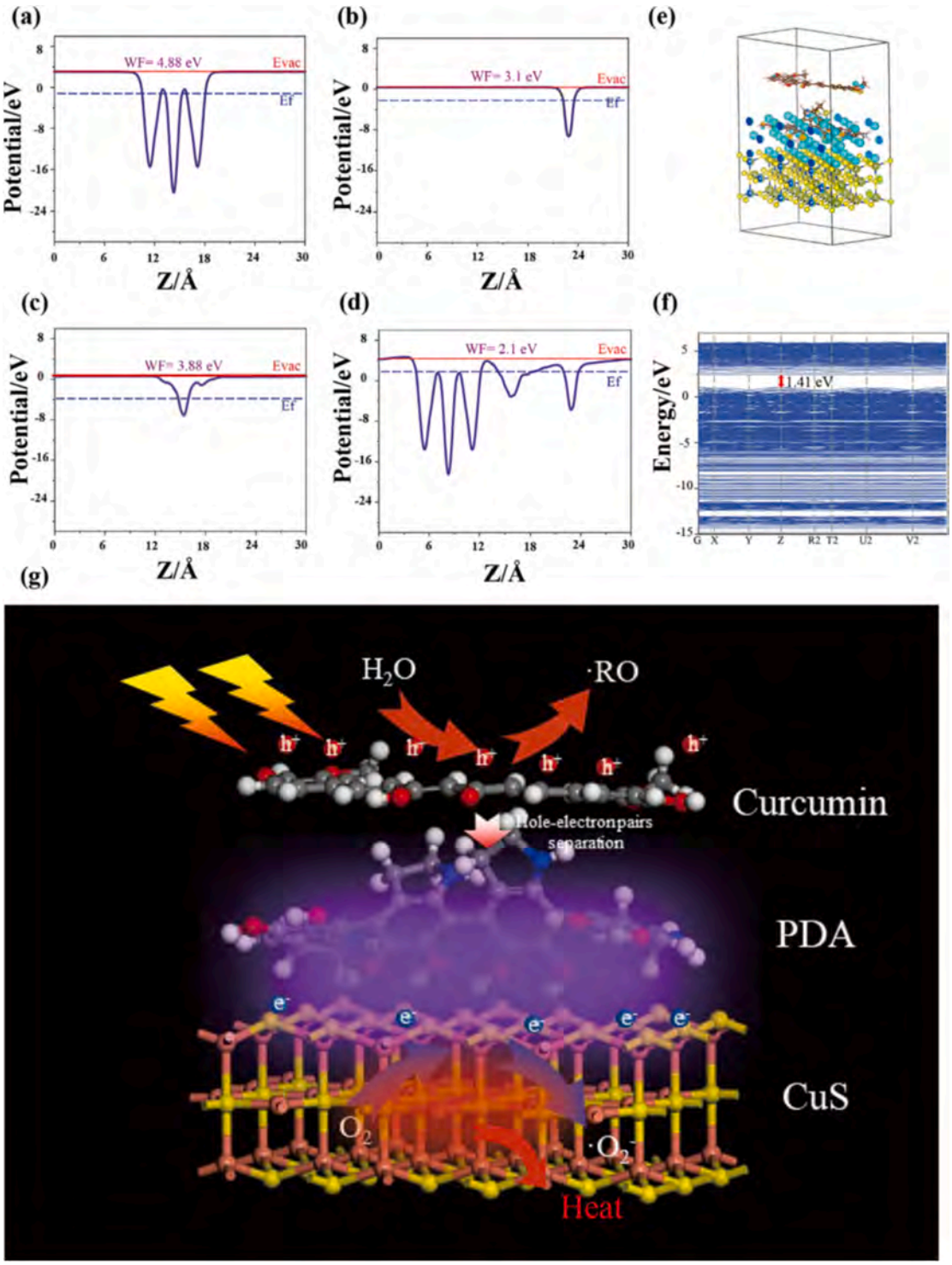


**Fig. 5.** Electrostatic potentials along the z-axis of (a) CuS, (b) curcumin (c) PDA and (d) CuS@C (Red solid lines denote the vacuum level ($E_{vac}$) and blue dashed lines represent the Fermi level ($E_F$)); (e) Charge density of CuS@C; (f) Electronic band structure of CuS@C; (g) Schematic diagram of the photodynamic and photothermal mechanism of CuS@C.

recombination of photo-generated electrons and holes. Therefore, compared to the CuS nanospheres, CuS@C produces ROS more effectively.

The interface charge transfer path and formation mechanism of CuS@C are further analyzed by DFT calculation. The WF calculation results of CuS, curcumin, and CuS@C nanospheres are shown in Fig. 5a-d. The WFs of CuS and curcumin are 4.88 eV and 3.1 eV, respectively. The electrostatic potential of curcumin is significantly higher than that of CuS, so that electrons of the curcumin molecule move spontaneously to the surface of the CuS nanospheres to form an interfacial electric field [39,40], which is also confirmed by the differential charge densities of CuS@C. The charge density distributions of curcumin, PDA, and CuS are shown in Fig. S8. Electrons on curcumin and PDA are uniformly distributed on the entire molecular structure due to delocalization, resulting in smaller reactivity of curcumin and PDA molecules [41]. Fig. 5e illustrates redistribution of electrons on the surface of CuS@C.

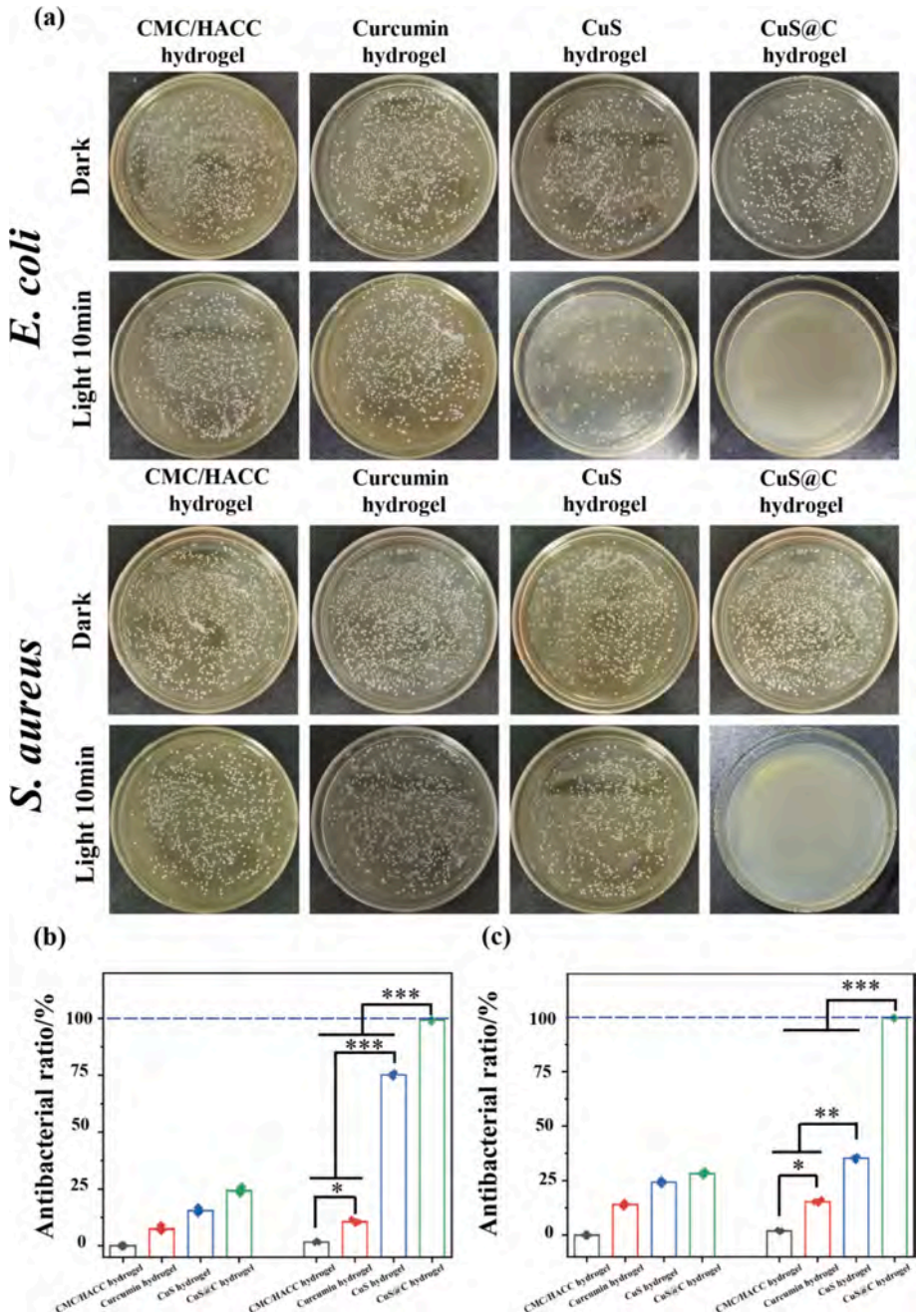


**Fig. 6.** (a) Photographs of *S. aureus* and *E. coli* colonies after treatment with the hydrogels with or without 808 nm laser irradiation; Antibacterial efficiency of the hydrogels against (b) *S. aureus* and (c) *E. coli*. (*p < 0.05, **p < 0.01, and ***p < 0.001).

The conjugated system of curcumin molecule is destroyed and electrons are transferred from the curcumin molecule to the surface of the CuS nanospheres. The curcumin molecule becomes an electron-deficient region and an electron-rich area is formed on the surface of the CuS nanospheres. Oxygen molecules can gain electrons in the electron-rich area to generate $\bullet O_2^-$, whereas water molecules lose electrons in the electron-deficient area to form •RO (Fig. 5g) [43]. The results indicate that the heterojunction composed of curcumin, PDA, and CuS nanospheres enhances production of ROS.

To better explain the influence of the formation of CuS@C on the catalytic process, the electron bandgap structure is simulated in Fig. 5f. The theoretical bandgap of CuS@C nanospheres is 1.41 eV indicating that formation of the heterojunction narrows the bandgap of the curcumin molecule (theoretical bandgaps of CuS and C are shown in Fig. S9). A small bandgap facilitates generation of more photogenerated electrons under the same irradiation conditions thereby increasing the yield of ROS.

GSH is an important antioxidant in bacterial cell membranes and can be converted into glutathione (GSSG) under oxidative conditions. To study the photocatalytic activity of the hydrogels incorporated with curcumin, CuS, and CuS@C, GSH is used. As shown in Fig. S10, the degradation rate of GSH in the curcumin hydrogel is extremely low suggesting weak photocatalytic activity. Meanwhile, curcumin cannot cause damage to bacterial cell membranes in a short time. In contrast, ROS and hyperthermia generated by the CuS nanospheres upon 808 nm laser irradiation degrade GSH and the degraded amount reaches 10.7 %. Owing to the improvement in the photocatalytic activity, the GSH degradation rate of the CuS@C hydrogel increases considerably to 37.2 % within 10 min.

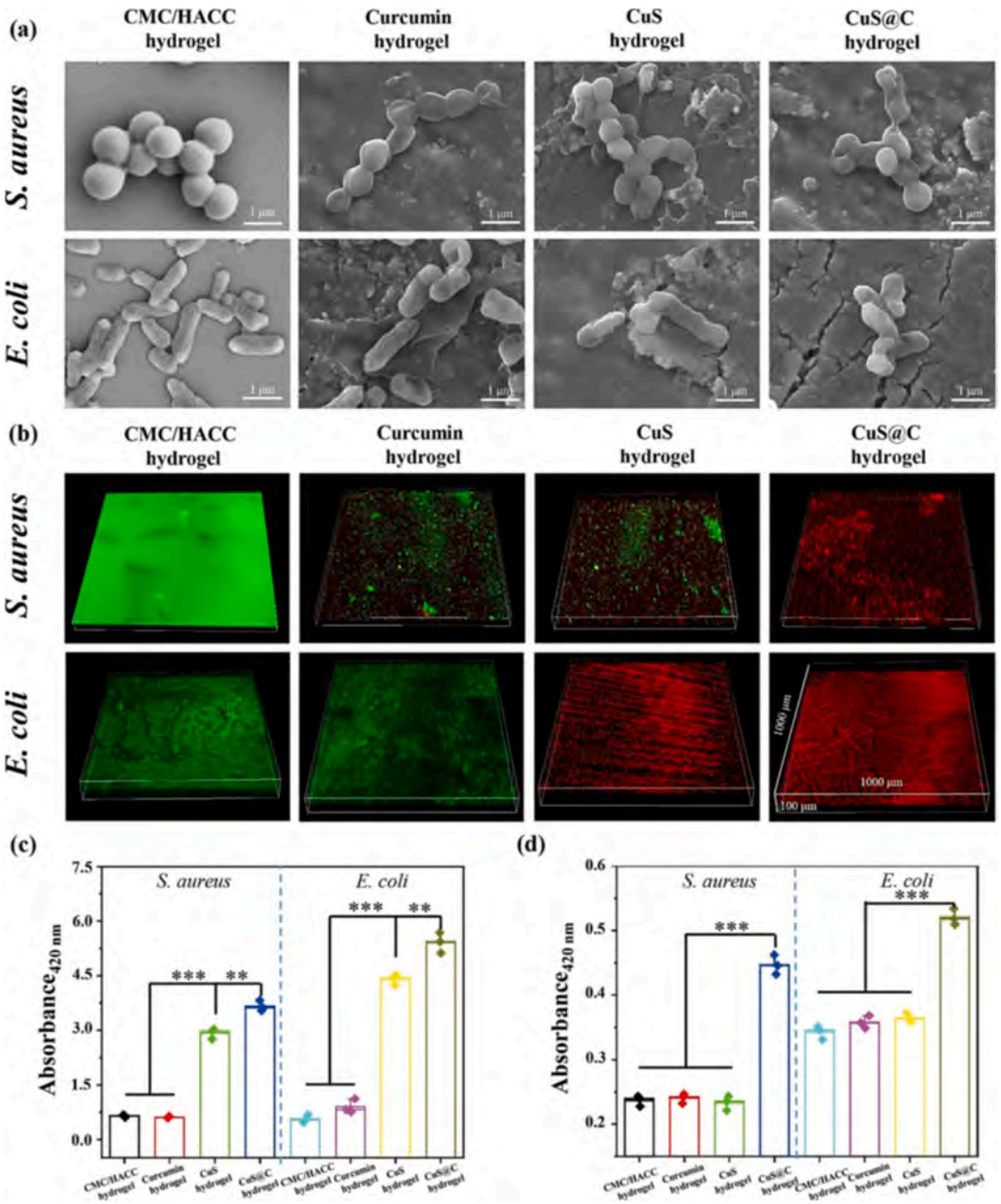


**Fig. 7.** (a) SEM images of the bacteria after treatment with the hydrogels upon 808 nm light irradiation for 10 min; (b) Fluorescence images of the biofilms after treatment with the hydrogels upon 808 nm laser irradiation for 10 min; (c) Bacterial membrane permeability and (d) Protein leakage of bacteria after treatment with the hydrogels upon 808 nm laser irradiation for 10 min. (**$p < 0.01$, ***$p < 0.001$).

### *3.4. In vitro antibacterial experiments*

The antibacterial activity of the hydrogels against *E. coli* (ATCC 10536) and *S. aureus* (*ATCC 25923*) is assessed by the spread plate method with the CMC/HACC hydrogel being the control group. Fig. S11 indicates that the relationship between CuS@C content and the antibacterial ability of hydrogels. The increase of CuS@C content can effectively improve the antibacterial efficiency of the hydrogel. When the content of CuS@C nanospheres in the hydrogel reaches 0.01 g, the CuS@C hydrogel can achieve 99.9 % antibacterial efficiency against *S. aureus* and *E. coli* under the irradiation of 808 nm NIR laser for 10 min. Therefore, 0.01 g of CuS@C is used in subsequent experiments based on the balance of bactericidal ability and biocompatibility. As shown in Fig. 6, all the hydrogels exhibit negligible antibacterial activities without light irradiation after incubation for 10 min, meaning that the small amount of released curcumin and $Cu^{2+}$ cannot reach the minimal inhibitory concentration (MIC) and exert the antimicrobial effects within a short time [44]. Curcumin is a traditional herbal medicine with antibacterial activity by inhibiting FtsZ protein polymerization in bacteria [45], but the bactericidal activity is weak. At the same time, curcumin is also a photosensitizer that can generate ROS under light conditions [46,47]. However, the curcumin hydrogel still does not have effective antibacterial properties upon 808 nm laser irradiation for 10 min. The antibacterial efficiencies of curcumin hydrogel are only 3.5 % and 4.8 % against *S. aureus* and *E. coli*, respectively. This is because curcumin has almost no light absorption in the NIR wavelength range and curcumin hydrogel cannot generate ROS during 808 nm laser irradiation to destroy bacteria. Upon 808 nm laser irradiation, the antibacterial efficiencies of the CuS hydrogel against *S. aureus* and *E. coli* are 35.2 % and 71.3 %, respectively, indicating that the generated ROS and

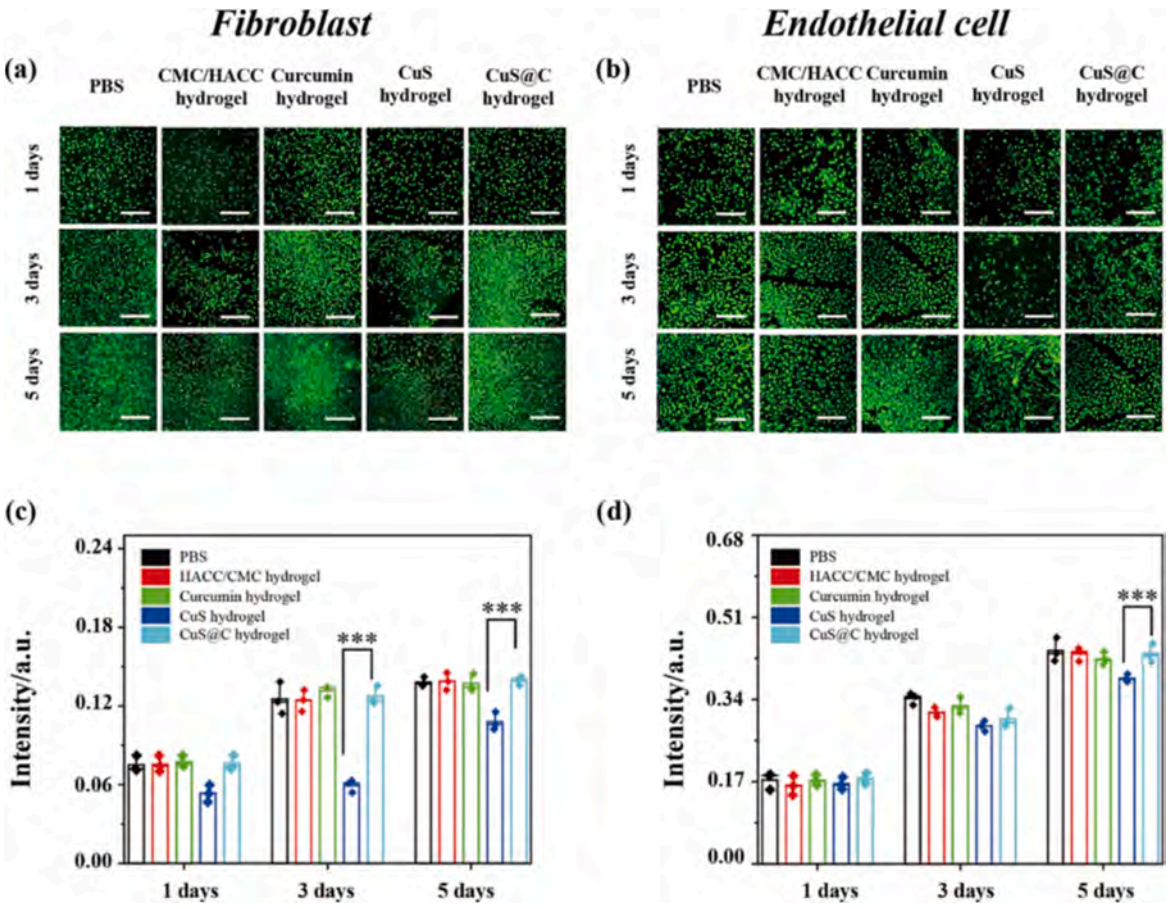


**Fig. 8.** Fluorescence images after live/dead staining of (a) Fibroblasts and (b) Endothelial cells after culturing for 1, 3 and 5 days; MTT assays of (c) Fibroblasts and (d) Endothelial cells. (**p < 0.01 and ***p < 0.001).

hyperthermia by CuS show some antibacterial activity. As expected, the CuS@C hydrogel has the best antibacterial properties with efficacies of 99.7 % and 99.9 % against *S. aureus* and *E. coli*, respectively. This is because the p-n junction composed of CuS and curcumin improves the photocatalytic activity and the synergistic effects rendered by ROS and hyperthermia produce the excellent antibacterial activity.

After exposure to the 808 nm laser for 10 min, the morphology of bacteria is observed by SEM (Fig. 7a). The bacteria of the control group retain the complete membrane structure without obvious shrinkage and deformation. The bacteria do not exhibit obvious deformation in the curcumin group either due to the weak antibacterial activity. However, severely distorted bacteria are found from both the CuS and CuS@C groups.

The antibacterial effects of the hydrogels against *S. aureus* and *E. coli* are evaluated by Live/Dead fluorescence staining and the results after exposure to the 808 nm laser for 10 min are displayed in Fig. 7b [48]. The surface of the control group shows green fluorescence. In the curcumin group, some red spots are found and more dead bacteria are observed from the CuS group. In contrast, nearly no green spots are observed from the CuS@C group indicating excellent antibacterial activity.

The permeability of the bacterial membrane is measured by ONPG [49,50]. When the cell membrane is ruptured, ONPG can be decomposed to *o*-nitrophenol by the *β*-galactosidase produced by the bacteria. As shown in Fig. 7c, after the light treatment, there is no obvious difference in the $OD_{420}$ values of both *S. aureus* and *E. coli* between the curcumin hydrogel and control group, indicating that the permeability of the bacterial membrane of the curcumin group does not change significantly. In comparison, hydrolysis of ONPG produced by the CuS hydrogel increases as shown by the relatively large $OD_{420}$ and the permeability of the bacterial membrane of the CuS@C group is further improved indicating that the combination of ROS and hyperthermia plays a major role in the bacterial membrane permeability. The higher cell permeability can cause leakage of proteins leading to bacteria death. As shown in Fig. 7d, the results of protein leakage reveal a similar trend as ONPG hydrolysis demonstrating the synergistic effects of photothermal and photodynamic on bacteria.

The anti-biofilm activity is measured by the crystal violet staining method and results after exposure to the 808 nm laser for 10 min are exhibited in Fig. S12. The OD value of CuS@C hydrogel group is significantly lower than that of CMC / HACC hydrogel group, curcumin hydrogel group and CuS hydrogel group. The results strongly prove that CuS@C hydrogel can cause effective damage to bacterial biofilms.

### 3.5. Biocompatibility

The biocompatibility of wound dressings is an essential factor in effective treatment. The biocompatibility of the hydrogels is tested using two typical cells (fibroblasts (NIH-3 T3) and endothelial cells (EA. Hy 926)) that are involved in wound healing. As shown in Fig. 8a and 8b, the fluorescence images of fibroblasts and endothelial cells reveal that the PBS, CMC/HACC and curcumin hydrogel groups have excellent biocompatibility. In contrast, the proliferation of fibroblasts and endothelial cells are inhibited due to excessive release of $Cu^{2+}$ in the CuS hydrogel group [51,52]. As for the CuS@C hydrogel group, the number of cells shows only a small decline with a survival rate of over 90 %. After 3 days, the survival rate of cells in the CuS@C hydrogel group is similar to that of the PBS and CMC/HACC hydrogel group, proving that modification of PDA and curcumin improves the biocompatibility of the CuS@C hydrogel. The quantitative results of cell viability are obtained

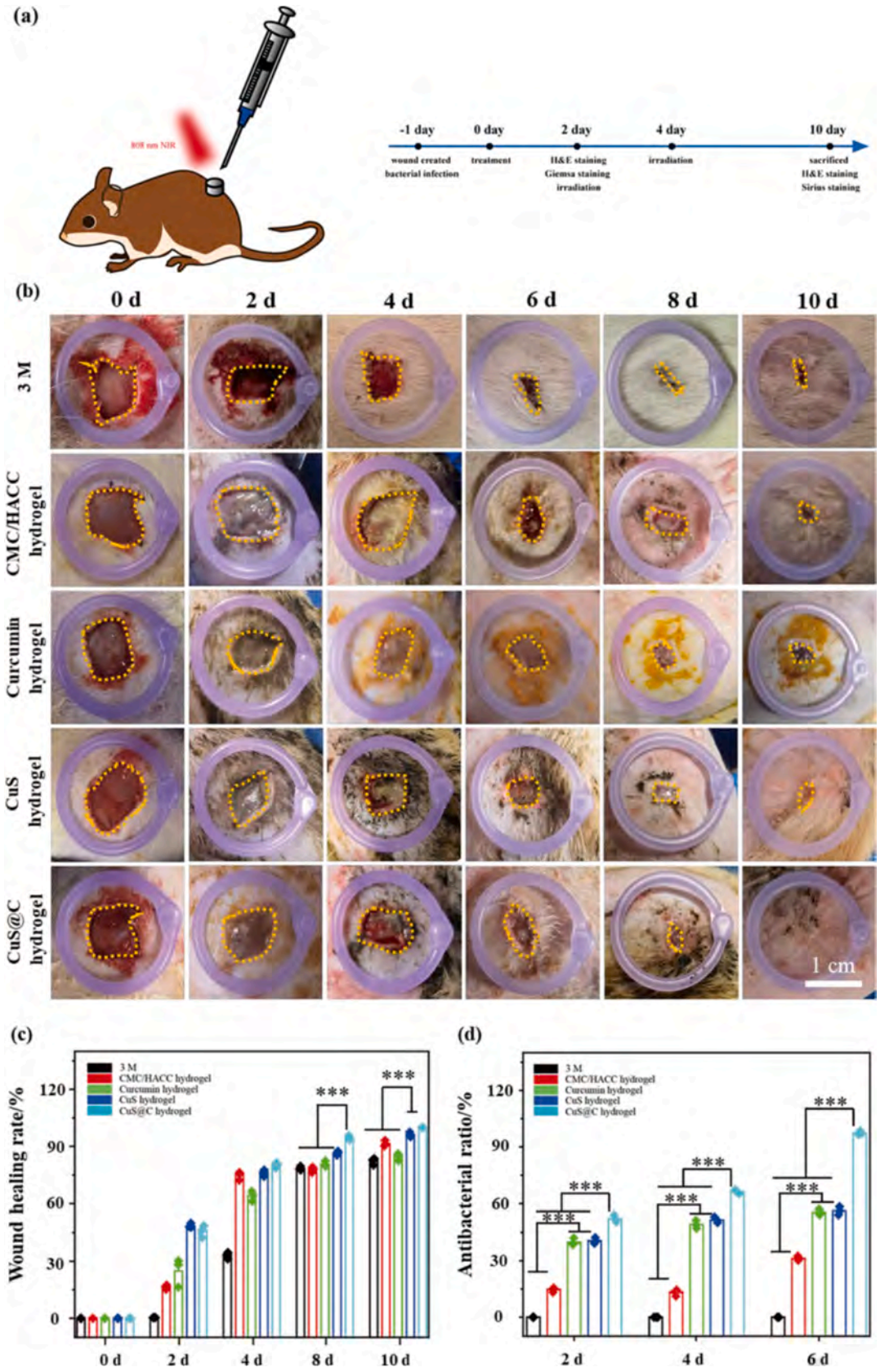


**Fig. 9.** (a) Schematic illustration of the *S. aureus* infection wound model and therapy; (b) Representative photographs of the infected wounds on days 0, 2, 4, 6, 8 and 10; (c) Wound healing rates; (d) Antibacterial rates of the hydrogels on days 2, 4, and 6 (***$p < 0.001$).

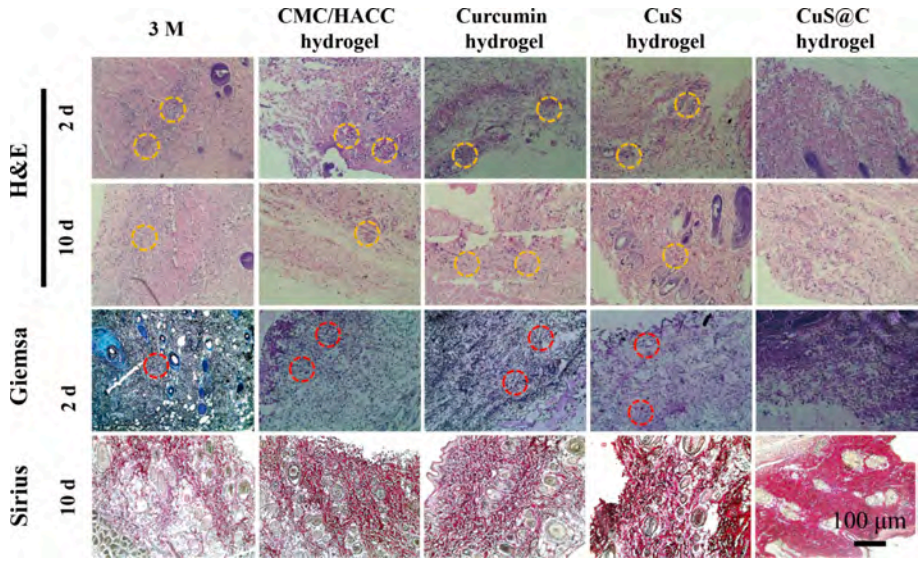


**Fig. 10.** H&E, Giemsa, and Sirius red staining images of the skin tissues around the wounds.

using the MTT assay. As shown in Fig. 8c and 8d, cell proliferation of the CuS hydrogel group decreases, whereas only a slight decrease is observed from the CuS@C hydrogel group compared to the control group. The results are consistent with fluorescence staining confirming the good biocompatibility of the CuS@C hydrogels quantitatively.

### 3.6. Animal experiments

A high temperature can damage cells and a temperature of 50 °C has been shown to inhibit cellular activity [48]. Hence, the antibacterial activity of the CuS@C hydrogel is investigated at a relatively low temperature (45 ℃) (Fig. S13). The CuS@C hydrogel still exhibits effective bacteria-killing efficacy of 98.8 % against *E. coli*. Although the antibacterial activity against *S. aureus* decreases to a certain extent at 45 ℃, the antibacterial efficiency still reaches 80.2 %. The antibacterial activity is also revealed by live/dead staining (Fig. S14) and the maximum temperature is controlled to be about 45 ℃ in the *in vivo* antibacterial assay.

A 1 cm × 1 cm infected wound is created at the back of the rats (SD rats, 300–350 g) to simulate the wound healing process of the CuS@C hydrogel [49,50]. The standard 3 M wound dressing serves as the control. After covering the infected wound with hydrogels, the hydrogels are irradiated with the 808 nm laser for 10 min. The temperature change is recorded *in vivo* recorded by a FLIR infrared thermal imager and the temperature curve is shown in Fig. S15. The temperature of the CuS hydrogel and CuS@C hydrogel rises beyond 45.4 ℃ within 4 min under 808 nm laser irradiation, while the CMC/HACC hydrogel and curcumin hydrogel do not exhibit significant temperature changes. The results indicate that CuS has excellent photothermal conversion effects *in vivo*. The representative photographs of the wound healing process show significant differences between the CuS@C group and other groups as shown in Fig. 9b. On the 2nd day, severe infection with ichor appears from the wound area of the mice in the control, curcumin hydrogel, and CuS hydrogel groups. The ichor is extracted from the wound area, transferred to an agar medium, and cultured for 12 h (Fig. S16). Not surprisingly, numerous colonies appear from the agar plates of the control, curcumin hydrogel, and CuS hydrogel groups. However, as for the CuS@C hydrogel group, no obvious ichor is observed from the wound area. The agar plates corresponding to CuS@C hydrogel also indicate that the antibacterial rate of CuS@C is 44.7 %, which is apparently higher than those of other groups. After three treatments with the 808 nm laser in 6 days, only a few viable colony units remain on the agar plate, but a large number of viable colony units remain on the agar plates of the other groups. These results prove that the CuS@C hydrogel has good antibacterial effects *in vivo*. After 8 days, the wound healing process with the CuS@C hydrogel is promoted significantly compared to the other groups due to the synergistic antibacterial effects of both PDT and PTT. The wound healing rate of the CuS@C hydrogel group reaches 93.3 % compared to that of the CMC/HACC hydrogel group of only 78.4 %. After 10 days, the wound in the CuS@C hydrogel group heals totally without leaving a scar, but the unhealed wound can still be observed from the other groups. The results provide strong evidence that the CuS@C hydrogel has the ability to kill bacteria and promote wound healing.

H&E staining and Giemsa staining of the wound tissues is performed on days 2 and 10 to confirm the antibacterial properties and wound healing activity of the hydrogels (Fig. 10). For the control group, CMC/HACC group, curcumin group, and CuS group, more inflammatory cells are observed from the wounds (marked by yellow arrows). This corresponding to the inflammatory response of serious wound infection, but it does not occur in the CuS@C hydrogel group. Giemsa staining indicates that the bacteria (marked by red arrows) in the CuS@C hydrogel group decrease compared to the other groups, proving that the CuS@C hydrogel has good antibacterial ability during wound treatment. Sirius red staining is used to assess the formation of collagen fibers as shown in Fig. 10. On the 10th day, the collagen fibers deposited on the skin tissues of the CuS@C hydrogel group are denser and more organized indicating that the CuS@C hydrogel has an excellent ability to promote wound healing.

The biosafety of the CuS@C hydrogels is evaluated by H&E staining of the major organs (heart, liver, spleen, lung, and kidney) in the mice (Fig. S17). Compared to the control group, the CMC/HACC hydrogel group, C hydrogel group, CuS hydrogel group, and CuS@C hydrogel group do not show severe damage of the major organs, proving that the CuS@C hydrogel group has high biosafety *in vivo*.

## 4. Conclusion

A wound dressing with enhanced NIR photodynamic and photothermal antibacterial activity is prepared by hybridizing synthetic CuS nanospheres with herbal medicine and natural organic macromolecules. The hybrid hydrogel has good injectability, self-healing ability, and degradation behavior. CuS usually possesses weak photocatalytic property under the irradiation of NIR light due to the narrow energy gap. The internal electric field at the interface between CuS and curcumin promotes NIR light utilization, enhances the mobility of electrons,

accelerates charge separation, and favors generation of ROS to kill bacteria. The hybrid hydrogels have excellent antibacterial properties *in vitro* and *in vivo* upon irradiation with 808 light for 10 min. Furthermore, the organic layer immobilized on the surface of the CuS nanospheres mitigates release of $Cu^{2+}$ to endow the CuS@C hydrogel with good biocompatibility. The *in vivo* experiments demonstrate that the organic/inorganic hybrid hydrogel is more effective than when they are used individually to accelerate infected wound healing.

## Declaration of Competing Interest

The authors declare that they have no known competing financial interests or personal relationships that could have appeared to influence the work reported in this paper.

## Data availability

Data will be made available on request.

## Acknowledgements

This work was financially supported by the National Natural Science Foundation of China (52171240, 82172503 and U21A20353), Postdoctoral Science Foundation of China (2021M691992), Major Projects in Research and Development of Shanxi (Projects of International Cooperation, 201803D421090), Shenzhen – Hong Kong Innovative Collaborative Research and Development Program (SGLH20181109110802117 and CityU 9240014), as well as City University of Hong Kong Donation Research Grant (DON-RMG 9229021).

## Appendix A. Supplementary data

Supplementary data to this article can be found online at https://doi.org/10.1016/j.cej.2022.139474.

## References

[1] G. Zhang, Y. Yang, J. Shi, X. Yao, W. Chen, X. Wei, X. Zhang, P.K. Chu, Near-infrared light II - assisted rapid biofilm elimination platform for bone implants at mild temperature, Biomaterials 269 (2021), 120634.
[2] Y. Yu, Y. Cheng, L. Tan, X. Liu, Z. Li, Y. Zheng, T. Wu, Y. Liang, Z. Cui, S. Zhu, S. Wu, Theory-screened MOF-based single-atom catalysts for facile and effective therapy of biofilm-induced periodontitis, Chem. Eng. J. 133279 (2021).
[3] B. Huang, X. Liu, Z. Li, Y. Zheng, K. Wai Kwok Yeung, Z. Cui, Y. Liang, S. Zhu, S. Wu, Rapid bacteria capturing and killing by AgNPs/N-CD@ZnO hybrids strengthened photo-responsive xerogel for rapid healing of bacteria-infected wounds, Chem. Eng. J. 414 (128805) (2021).
[4] G. Zhang, Z. Wu, Y. Yang, J. Shi, J. Lv, Y. Fang, Z. Shen, Z. Lv, P. Li, X. Yao, W. Chen, X. Wei, P.K. Chu, X. Zhang, A multifunctional antibacterial coating on bone implants for osteosarcoma therapy and enhanced osteointegration, Chem. Eng. J. 428 (2022), 131155.
[5] Y. Liu, Y. Tian, Q. Han, J. Yin, J. Zhang, Y. Yu, W. Yang, Y. Deng, Synergism of 2D/1D MXene/cobalt nanowire heterojunctions for boosted photo-activated antibacterial application, Chem. Eng. J. 410 (2021), 128209.
[6] J. Li, Y. Wang, J. Yang, W. Liu, Bacteria activated-macrophage membrane-coated tough nanocomposite hydrogel with targeted photothermal antibacterial ability for infected wound healing, Chem. Eng. J. 420 (2021), 127638.
[7] L. Feng, S. Wu, Y. Wu, Intracellular bottom-up synthesis of ultrasmall CuS nanodots in cancer cells for simultaneous photothermal therapy and $CO_{X-2}$ inactivation, Adv. Funct. Mater. 31 (27) (2021) 2101297.
[8] Z. Zheng, P. Yu, H. Cao, M. Cheng, T. Zhou, L.E. Lee, J. Ulstrup, J. Zhang, C. Engelbrekt, L. Ma, Starch capped atomically thin CuS nanocrystals for efficient photothermal therapy, Small 17 (47) (2021) 2103461.
[9] X. Zhang, G. Zhang, H. Zhang, X. Liu, J. Shi, H. Shi, X. Yao, P.K. Chu, X. Zhang, A bifunctional hydrogel incorporated with CuS@$MoS_2$ microspheres for disinfection and improved wound healing, Chem. Eng. J. 382 (2020), 122849.
[10] M. Zhang, X. Qin, W. Xu, Y. Wang, Y. Song, S. Garg, Y. Luan, Engineering of a dual-modal phototherapeutic nanoplatform for single NIR laser-triggered tumor therapy, J Colloid Interf Sci 594 (2021) 493–501.
[11] L. Zhou, S. Dai, S. Xu, Y. She, Y. Li, S. Leveneur, Y. Qin, Piezoelectric effect synergistically enhances the performance of $Ti_{32}$-oxo-cluster/$BaTiO_3$/CuS p-n heterojunction photocatalytic degradation of pollutants, Appl Catal B: Environ 291 (2021), 120019.
[12] P. Wang, Y. Gao, P. Li, X. Zhang, H. Niu, Z. Zheng, Doping Zn2+ in CuS nanoflowers into chemically homogeneous $Zn_{0.49}Cu_{0.50}S_{1.01}$ superlattice crystal structure as high-efficiency n-type photoelectric semiconductors, ACS Appl. Mater. Interfaces 8 (24) (2016) 15820–15827.
[13] L. Guo, I. Panderi, D.D. Yan, K. Szulak, Y. Li, Y. Chen, H. Ma, D.B. Niesen, N. Seeram, A. Ahmed, B. Yan, D. Pantazatos, W. Lu, A Comparative Study of Hollow Copper Sulfide Nanoparticles and Hollow Gold Nanospheres on Degradability and Toxicity, ACS Nano 7 (10) (2013) 8780–8793.
[14] M. Zhang, X. Liu, Q. Luo, Q. Wang, L. Zhao, G. Deng, R. Ge, L. Zhang, J. Hu, J. Lu, Tumor environment responsive degradable CuS@m$SiO_2$@$MnO_2$/DOX for MRI guided synergistic chemo-photothermal therapy and chemodynamic therapy, Chem. Eng. J. 389 (2020), 124450.
[15] X. Pan, P. Li, L. Bai, J. Ma, S. Li, F. Zhang, S. Liu, Q. Wu, H. Shen, H. Liu, Biodegradable nanocomposite with dual cell-tissue penetration for deep tumor chemo-phototherapy, Small 16 (22) (2020) 2000809.
[16] J. Zhu, W. Wang, X. Wang, L. Zhong, X. Song, W. Wang, Y. Zhao, X. Dong, Multishell Nanoparticles with "Linkage Mechanism" for Thermal Responsive Photodynamic and Gas Synergistic Therapy, Adv Healthc Mater 10 (10) (2021) 2002038.
[17] T. Ouyang, J. Guo, H. Shen, M. Mu, Y. Shen, X. Yin, The Z-scheme transfer of photogenerated electrons for $CO_2$ photocatalytic reduction over g-ZnO/2H-$MoS_2$ heterostructure, Nanoscale 13 (43) (2021) 18192–18200.
[18] D. Ding, Y. Zhou, T. He, S. Rong, Facet selectively exposed α-$MnO_2$ for complete photocatalytic oxidation of carcinogenic HCHO at ambient temperature, Chem. Eng. J. 133737 (2021).
[19] T. Esatbeyoglu, P. Huebbe, I.M.A. Ernst, D. Chin, A.E. Wagner, G. Rimbach, Curcumin—from molecule to biological function, Angew. Chem. Int. Ed. 51 (22) (2012) 5308–5332.
[20] X. Zarate, P.I. González, S. Caramori, E. Benazzi, T. Barra, L. Arrue, Y. Wu, C. Díaz-Uribe, W. Vallejo, E. Schott, Experimental and DFT study of natural curcumin derived dyes as n-type sensitizers, Sol. Energy 225 (2021) 305–315.
[21] X. Jiang, Z. Yang, Y. Peng, B. Han, Z. Li, X. Li, W. Liu, Preparation, characterization and feasibility study of dialdehyde carboxymethyl cellulose as a novel crosslinking reagent, Carbohyd Polymers 137 (2016) 632–641.
[22] L. Jiang, Y. Li, X. Wang, L. Zhang, J. Wen, M. Gong, Preparation and properties of nano-hydroxyapatite/chitosan/carboxymethyl cellulose composite scaffold, Carbohyd Polym 74 (3) (2008) 680–684.
[23] Z. Yang, B. Yuan, X. Huang, J. Zhou, J. Cai, H. Yang, A. Li, R. Cheng, Evaluation of the flocculation performance of carboxymethyl chitosan-graft-polyacrylamide, a novel amphoteric chemically bonded composite flocculant, Water Res. 46 (1) (2012) 107–114.
[24] Z. Zhao, Q. Li, X. Qin, M. Zhang, Q. Du, Y. Luan, An injectable hydrogel reshaping adenosinergic axis for cancer therapy, Adv. Funct. Mater. 32 (24) (2022) 2200801.
[25] Q. Li, Z. Zhao, X. Qin, M. Zhang, Q. Du, Z. Li, Y. Luan, A Checkpoint-Regulatable Immune Niche Created by Injectable Hydrogel for Tumor Therapy, Adv. Funct. Mater. 31 (37) (2021) 2104630.
[26] Z. Wei, J.H. Yang, Z.Q. Liu, F. Xu, J.X. Zhou, M. Zrínyi, Y. Osada, Y.M. Chen, Novel biocompatible polysaccharide-based self-healing hydrogel, Adv. Funct. Mater. 25 (9) (2015) 1352–1359.
[27] J. Wen, Z. Jia, X. Zhang, M. Pan, J. Yuan, L. Zhu, Tough, thermo-Responsive, biodegradable and fast self-healing polyurethane hydrogel based on microdomain-closed dynamic bonds design, Mater. Today Commun. 25 (2020), 101569.
[28] K. Li, J. Wang, P. Li, Y. Fan, Ternary hydrogels with tunable mechanical and self-healing properties based on the synergistic effects of multiple dynamic bonds, J. Mater. Chem. B 8 (21) (2020) 4660–4671.
[29] C.J. Pan, J.J. Tang, Y.J. Weng, J. Wang, N. Huang, Preparation, characterization and anticoagulation of curcumin-eluting controlled biodegradable coating stents, J. Control. Release 116 (1) (2006) 42–49.
[30] S. Lu, J. Yu, Y. Cheng, Q. Wang, A. Barras, W. Xu, S. Szunerits, D. Cornu, R. Boukherroub, Preparation of silver nanoparticles/polydopamine functionalized polyacrylonitrile fiber paper and its catalytic activity for the reduction 4-nitrophenol, Appl. Surf. Sci. 411 (2017) 163–169.
[31] M.Y. Lucero, J. Chan, Photoacoustic imaging of elevated glutathione in models of lung cancer for companion diagnostic applications, Nat. Chem. 13 (12) (2021) 1248–1256.
[32] T.I. Kim, B. Kwon, J. Yoon, I. Park, G.S. Bang, Y. Park, Y. Seo, S. Choi, Antibacterial activities of graphene oxide–molybdenum disulfide nanocomposite films, ACS Appl Mater Inter 9 (9) (2017) 7908–7917.
[33] Y. Liang, Z. Li, Y. Huang, R. Yu, B. Guo, Dual-dynamic-bond cross-linked antibacterial adhesive hydrogel sealants with on-demand removability for post-wound-closure and infected wound healing, ACS Nano 15 (4) (2021) 7078–7093.
[34] J. Qu, X. Zhao, Y. Liang, Y. Xu, P.X. Ma, B. Guo, Degradable conductive injectable hydrogels as novel antibacterial, anti-oxidant wound dressings for wound healing, Chem. Eng. J. 362 (2019) 548–560.
[35] M.A. Cremonini, L. Lunazzi, G. Placucci, P.J. Krusic, Addition of alkylthio and alkoxy radicals to $C_{60}$ studied by ESR, J. Org. Chem. 58 (1993) 4735–4738.
[36] Q. Wu, L. Tan, X. Liu, Z. Li, Y. Zhang, Y. Zheng, Y. Liang, Z. Cui, S. Zhu, S. Wu, The enhanced near-infrared photocatalytic and photothermal effects of MXene-based heterojunction for rapid bacteria-killing, Appl Catal B-Environ 297 (2021), 120500.
[37] J. Li, Z. Li, X. Liu, C. Li, Y. Zheng, K.W.K. Yeung, Z. Cui, Y. Liang, S. Zhu, W. Hu, Y. Qi, T. Zhang, X. Wang, S. Wu, Interfacial engineering of $Bi_2S_3$/$Ti_3C_2T_x$ MXene based on work function for rapid photo-excited bacteria-killing, Nat. Commun. 12 (1) (2021) 1224.
[38] T.A. Wright, R.C. Page, D. Konkolewicz, Polymer conjugation of proteins as a synthetic post-translational modification to impact their stability and activity, Polym. Chem. 10 (4) (2019) 434–454.

[39] Y. Gao, Z. Chen, Y. Zhu, T. Li, C. Hu, New insights into the generation of singlet oxygen in the metal-free peroxymonosulfate activation process: important role of electron-deficient carbon atoms, Environ. Sci. Technol. 54 (2) (2020) 1232–1241.
[40] Y. Liu, M. Liu, M.T. Swihart, Reversible crystal phase interconversion between covellite CuS and high chalcocite $Cu_2S$ nanocrystals, Chem. Mater. 29 (11) (2017) 4783–4791.
[41] H. Liu, J. Li, X. Liu, Z. Li, Y. Zhang, Y. Liang, Y. Zheng, S. Zhu, Z. Cui, S. Wu, Photo-Sono interfacial engineering exciting the intrinsic property of herbal nanomedicine for rapid broad-spectrum bacteria killing, ACS Nano 15 (11) (2021) 18505–18519.
[42] S. Kaur, N.H. Modi, D. Panda, N. Roy, Probing the binding site of curcumin in Escherichia coli and Bacillus subtilis FtsZ – A structural insight to unveil antibacterial activity of curcumin, Eur. J. Med. Chem. 45 (9) (2010) 4209–4214.
[43] S. Zorofchian Moghadamtousi, H. Abdul Kadir, P. Hassandarvish, H. Tajik, S. Abubakar, K. Zandi, J.C.T. Carvalho, A review on antibacterial, antiviral, and antifungal activity of curcumin, Biomed Res. Int. 2014 (2014), 186864.
[44] Q. Qin, Z. Wei, Z. Wang, X. Huang, M. Tan, H. Zou, H. Liang, Imaging and therapeutic applications of Zn(ii)-cryptolepine–curcumin molecular probes in cell apoptosis detection and photodynamic therapy, Chem. Commun. 56 (28) (2020) 3999–4002.
[45] Y. Zhu, W. Hong, X. Liu, L. Tan, J. Wu, C. Mao, Y. Xiang, S. Wu, K.M.C. Cheung, K. W.K. Yeung, Rapid bacterial elimination achieved by sonodynamic Au@$Cu_2O$ hybrid nanocubes, Nanoscale 13 (37) (2021) 15699–15710.
[46] W. Cao, L. Yue, Y. Zhang, Z. Wang, Photodynamic chitosan functionalized $MoS_2$ nanocomposite with enhanced and broad-spectrum antibacterial activity, Carbohyd Polym 277 (2022), 118808.
[47] Y. Lu, L. Li, Y. Zhu, X. Wang, M. Li, Z. Lin, X. Hu, Y. Zhang, Q. Yin, H. Xia, C. Mao, Multifunctional copper-containing carboxymethyl chitosan/alginate scaffolds for eradicating clinical bacterial infection and promoting bone formation, ACS Appl Mater Inter 10 (1) (2018) 127–138.
[48] Y. Li, J. Wang, Y. Yang, J. Shi, H. Zhang, X. Yao, W. Chen, X. Zhang, A rose bengal/graphene oxide/PVA hybrid hydrogel with enhanced mechanical properties and light-triggered antibacterial activity for wound treatment, Mater. Sci. Eng., C 118 (2021), 111447.
[49] N.C. Cady, J.L. Behnke, A.D. Strickland, Copper-based nanostructured coatings on natural cellulose: nanocomposites exhibiting rapid and efficient inhibition of a multi-drug resistant wound pathogen, A. baumannii, and Mammalian Cell Biocompatibility in Vitro, Adv. Funct. Mater. 21 (13) (2011) 2506–2514.
[50] J. Li, X. Liu, L. Tan, Z. Cui, X. Yang, Y. Liang, Z. Li, S. Zhu, Y. Zheng, K.W.K. Yeung, X. Wang, S. Wu, Zinc-doped Prussian blue enhances photothermal clearance of Staphylococcus aureus and promotes tissue repair in infected wounds, Nat. Commun. 10 (1) (2019) 4490.
[51] C. Mao, Y. Xiang, X. Liu, Z. Cui, X. Yang, Z. Li, S. Zhu, Y. Zheng, K.W.K. Yeung, S. Wu, Repeatable photodynamic therapy with triggered signaling pathways of fibroblast cell proliferation and differentiation to promote bacteria-accompanied wound healing, ACS Nano 12 (2) (2018) 1747–1759.
[52] Y. Xiang, Q. Zhou, Z. Li, Z. Cui, X. Liu, Y. Liang, S. Zhu, Y. Zheng, K.W.K. Yeung, S. Wu, A Z-scheme heterojunction of ZnO/CDots/$C_3N_4$ for strengthened photoresponsive bacteria-killing and acceleration of wound healing, J. Mater. Sci. Technol. 57 (2020) 1–11.

# An injectable, self-healing composite hydrogel with enhanced near-infrared photo-antibacterial therapeutic effects for accelerated wound healing

Jiameng Wang [a], Hao Cheng [a], Weiyi Chen [b], Peide Han [c], Xiaohong Yao** [a], Bin Tang [a], Wangping Duan [d], Pengcui Li [d], Xiaochun Wei [d], Paul K Chu [e], Xiangyu Zhang* [a,b,d]

[a] Shanxi Key Laboratory of Biomedical Metal Materials, College of Materials Science and Engineering, Taiyuan University of Technology, Taiyuan 030024, China

[b] College of Biomedical Engineering, Taiyuan University of Technology, Taiyuan 030024, China

[c] College of Materials Science and Engineering, Taiyuan University of Technology, Taiyuan 030024, China

[d] Shanxi Key Laboratory of Bone and Soft Tissue Injury Repair, Department of Orthopedics, Second Hospital of Shanxi Medical University, Taiyuan 030001, China

[e] Department of Physics, Department of Materials Science and Engineering, and Department of Biomedical Engineering, City University of Hong Kong, Tat Chee Avenue, Kowloon, Hong Kong, China



*Corresponding Author: E-mail: zhangxiangyu@tyut.edu.cn (XY Zhang)
**Corresponding Author: E-mail: xhyao@tyut.edu.cn (XH Yao)

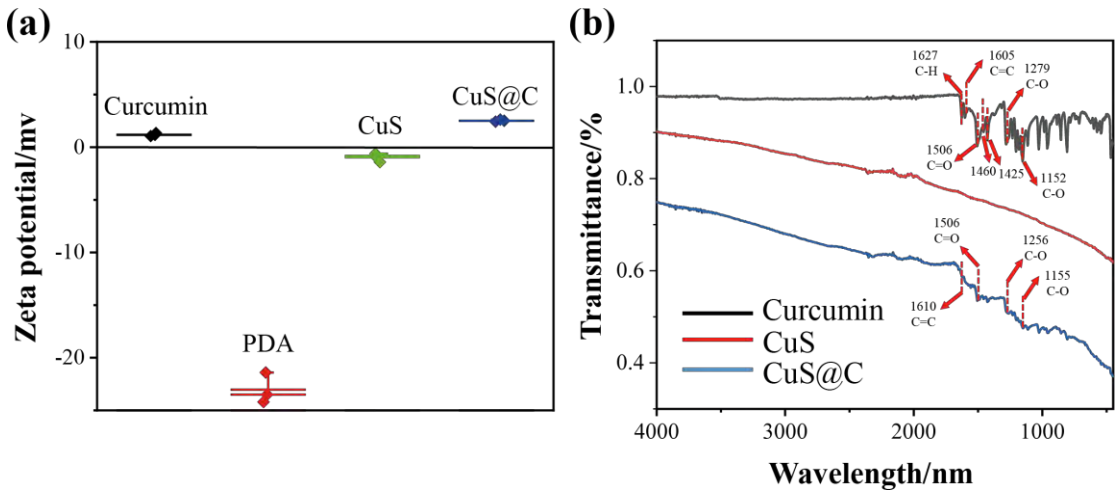


**Figure S1.** (a) Zeta potentials of curcumin, PDA, CuS, and CuS@C nanospheres and (b) FT-IR spectra of curcumin, CuS, and CuS@C nanospheres.

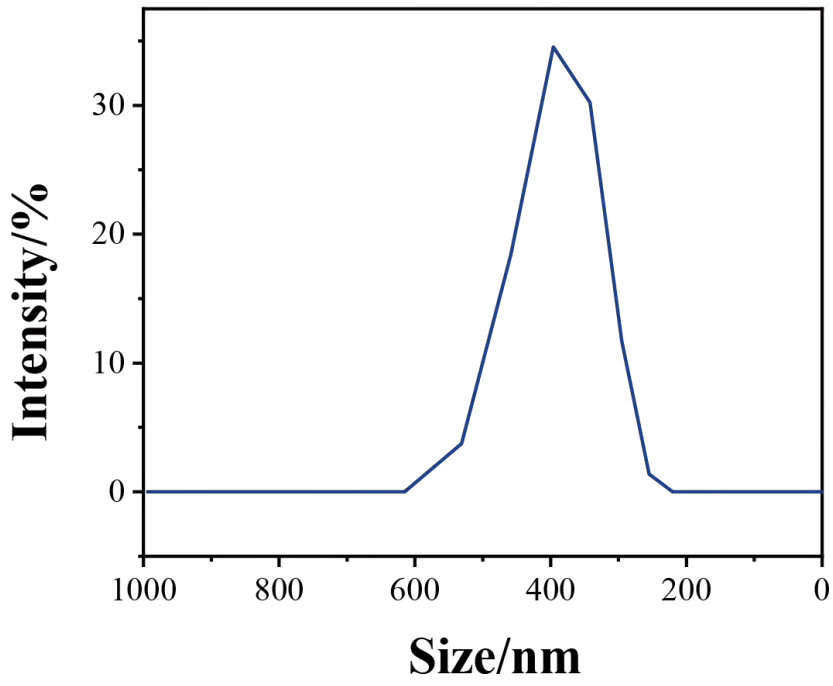


**Figure S2.** Size distribution of CuS@C nanospheres.

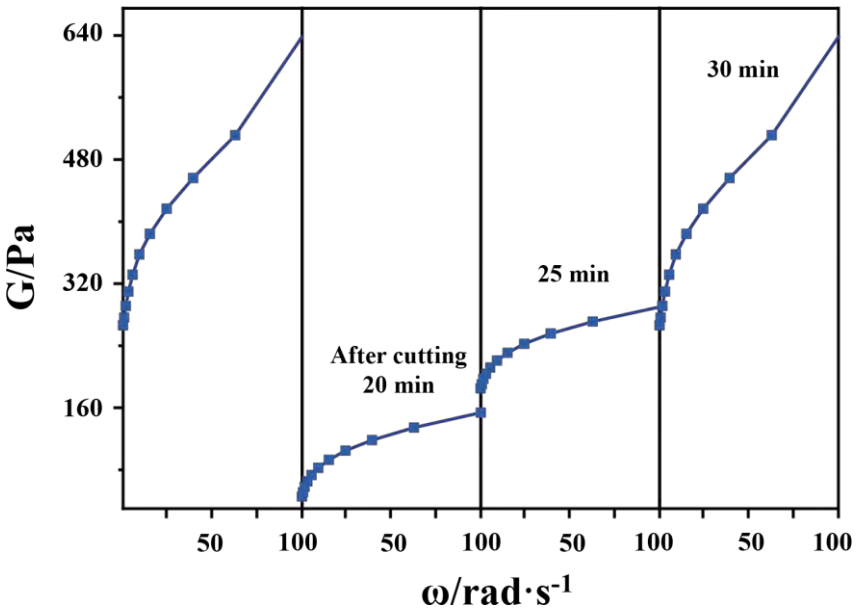


Figure S3. The rheological property of CuS@C hydrogel.

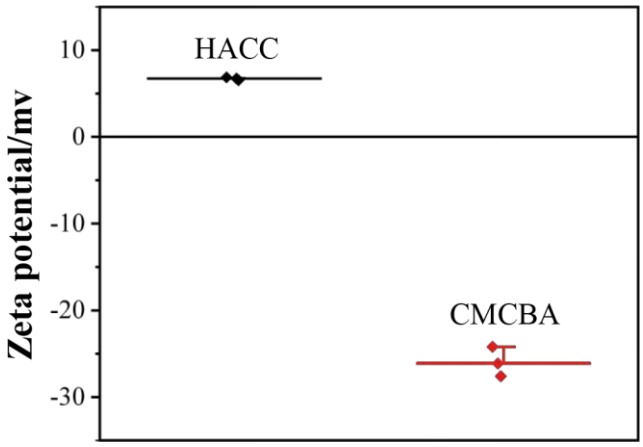


**Figure S4.** Zeta potentials of HACC and CMCBA molecules.

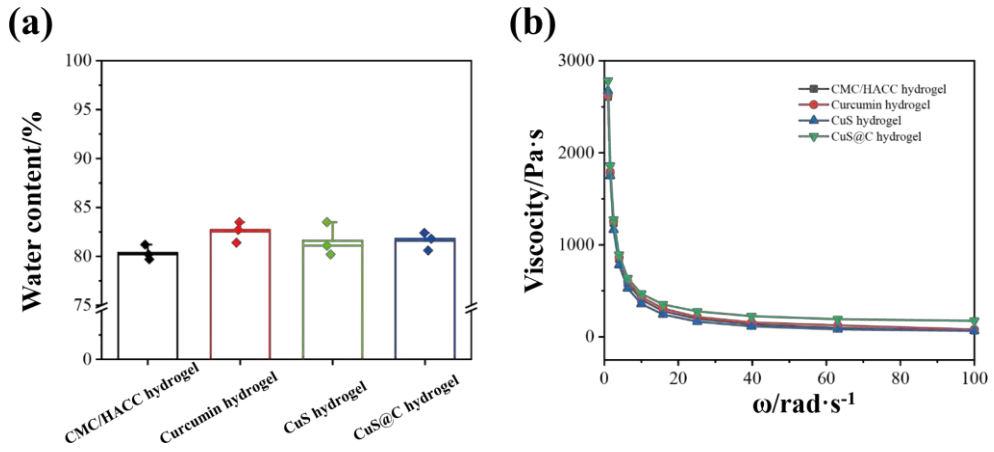


Figure S5. (a) Water content of the hydrogels; (b) The viscosity of the hydrogels.

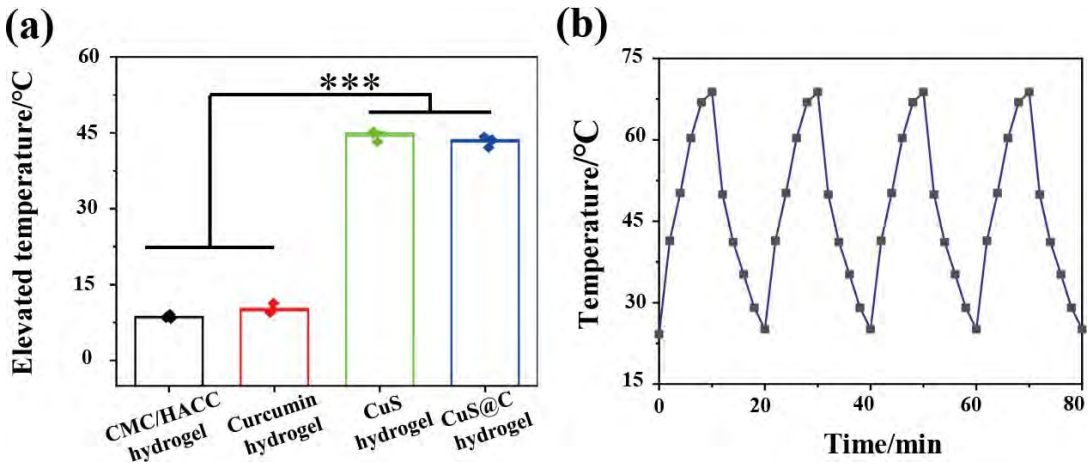


**Figure S6.** (a) Elevated temperature after irradiation for 10 min; (b) Heating/cooling profiles of CuS@C hydrogel for 4 cycles (***$p < 0.001$).

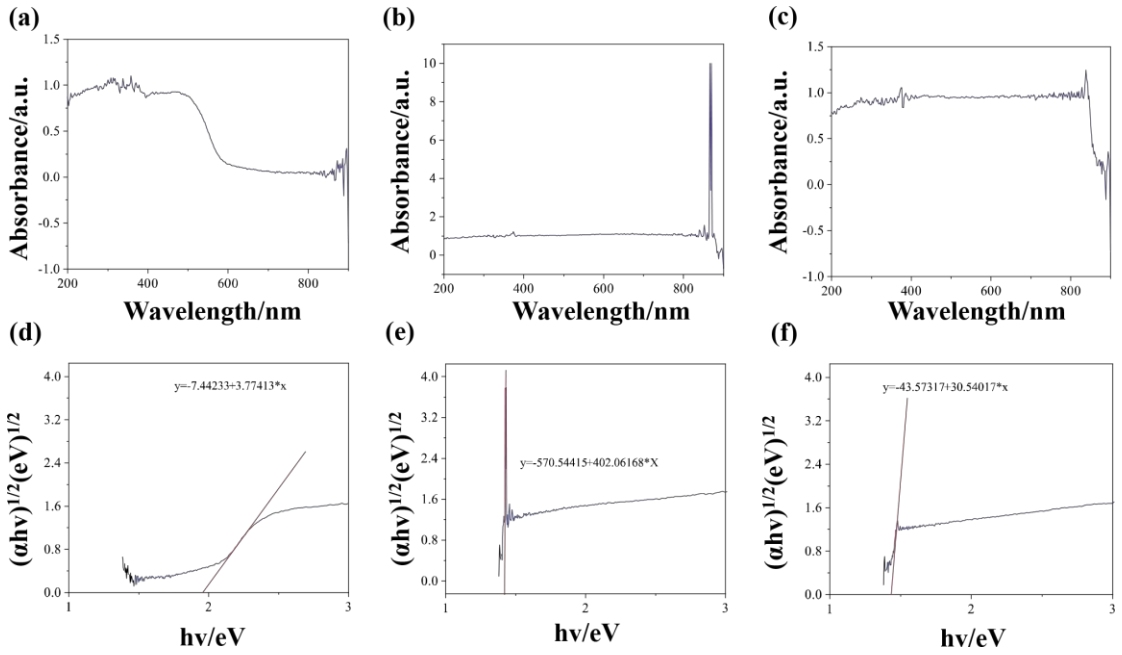


**Figure S7.** UV-vis-NIR diffuse reflectance spectra of (a) Curcumin, (b) CuS. and (c) CuS@C; Bandgaps of (d) Curcumin, (e) CuS and (f) CuS@C calculated from the UV-vis-NIR diffuse reflectance spectra.

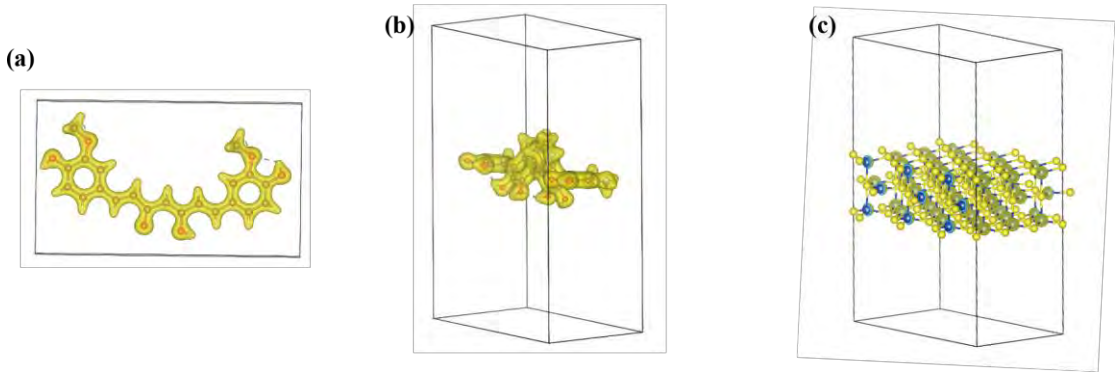


**Figure S8.** Charge densities of (a) Curcumin, (b) PDA, and (c) CuS nanospheres.

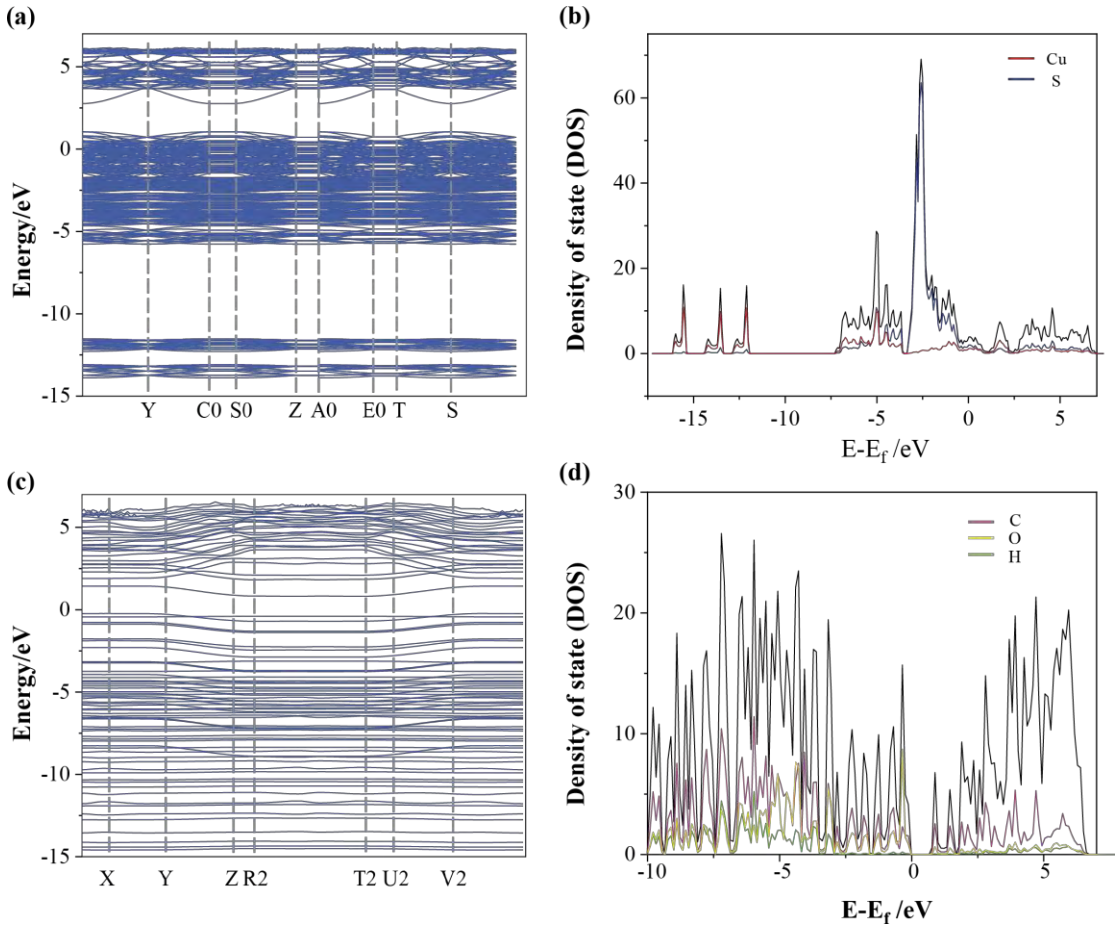


**Figure S9.** (a) Electronic band structure and (b) DOS of CuS; (c) Electronic band structure and (d) DOS of curcumin.

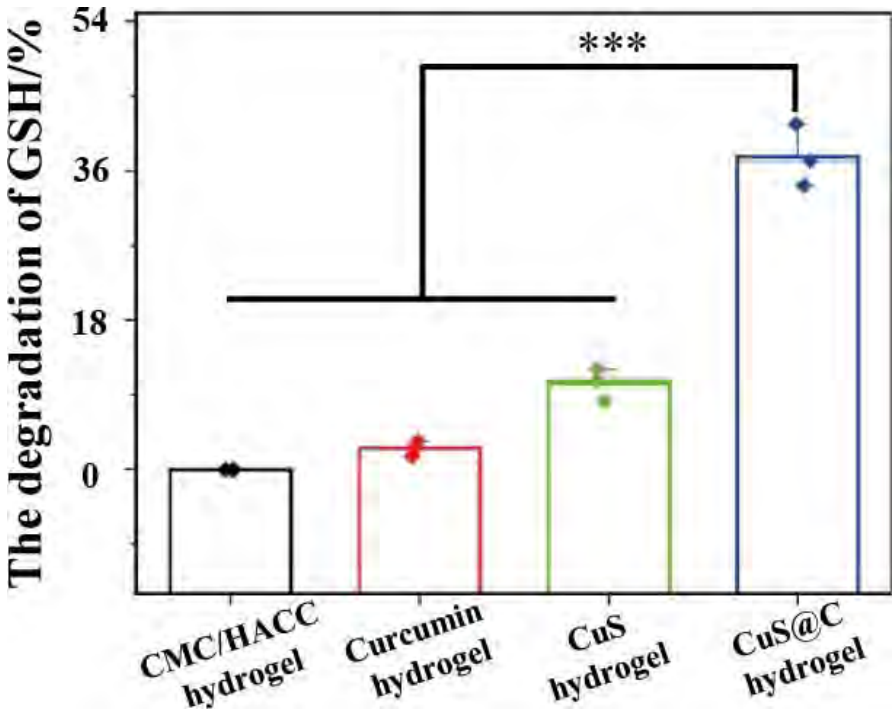


**Figure S10.** Loss of GSH after treatment with hydrogels under 808 nm light irradiation for 10 minutes (***$p < 0.001$).

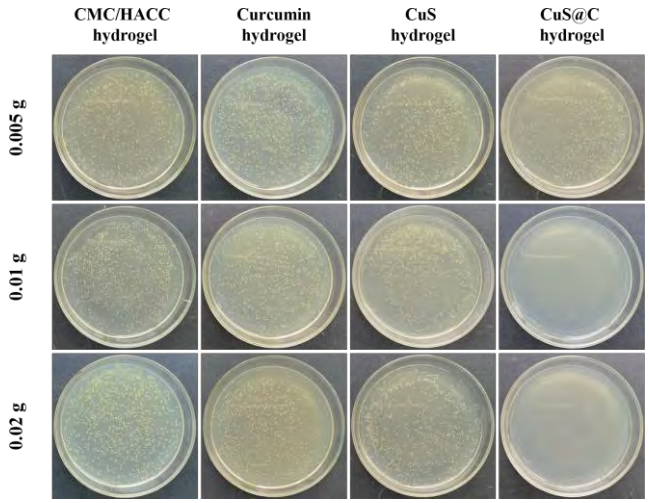


**Figure S11.** Photographs of *S. aureus* colonies of hydrogels with various CuS@C nanosphere contents

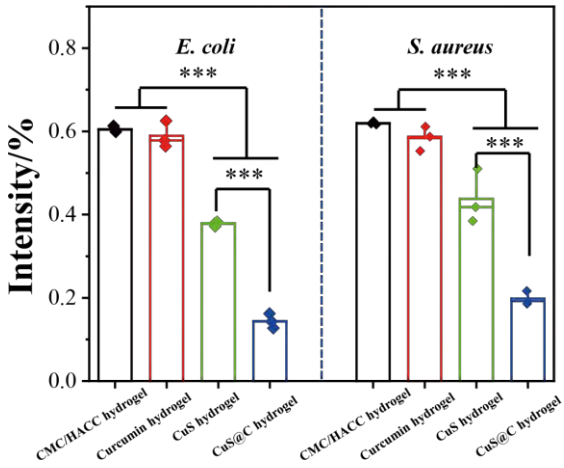


**Figure S12.** The anti-biofilm assay of the hydrogels against *E. coli* and *S. aureus*.

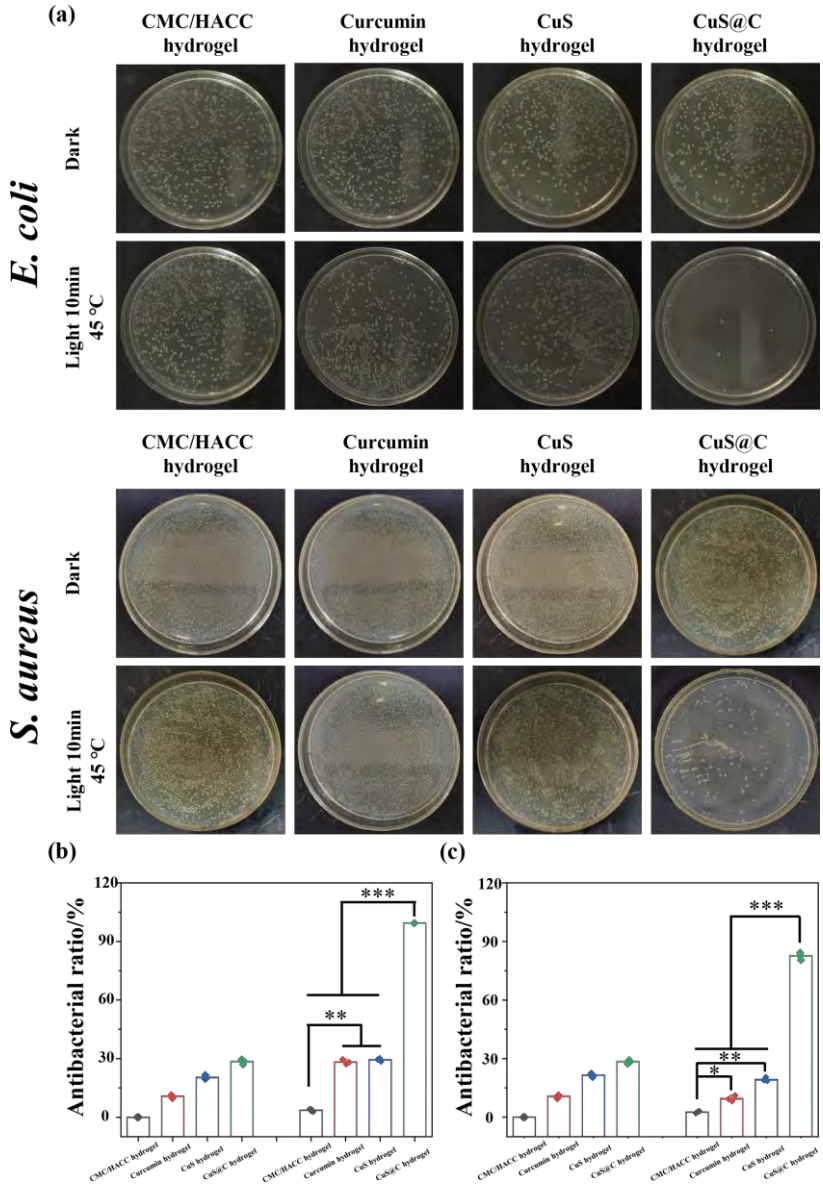


**Figure S13.** (a) Photographs of *S. aureus* and *E. coli* colonies treated with hydrogels

with or without 808 nm NIR irradiation at temperature below 45°C; Antibacterial efficiency of hydrogels against (b) *S. aureus* and (c) *E. coli* at temperature below 45 °C (*p < 0.05, **p < 0.01, and ***p < 0.001).

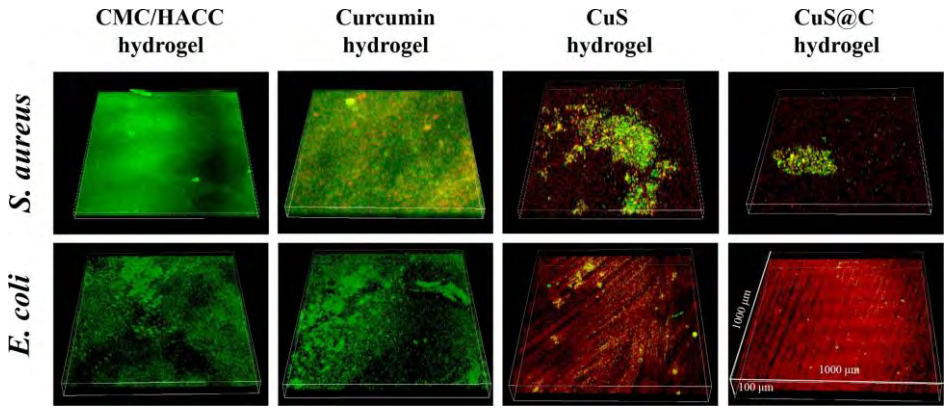


**Figure S14.** Fluorescence images of S. aureus and E. coli biofilms irradiated with 808 nm NIR at 45 °C for 10 minutes.

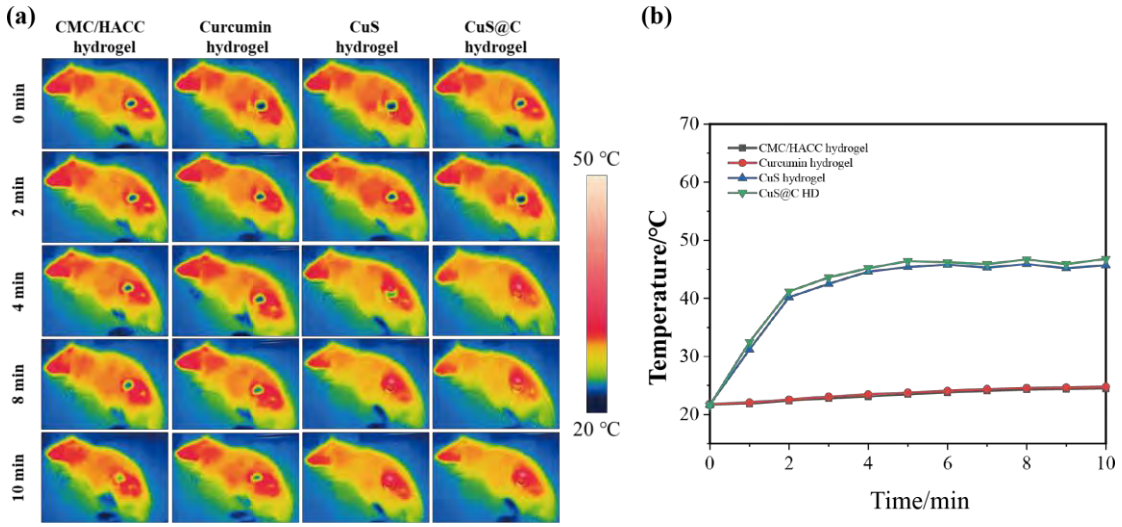


**Figure S15.** (a) Photothermal images of hydrogels after *in vivo* experiments and (b) Corresponding heating curves of hydrogels.

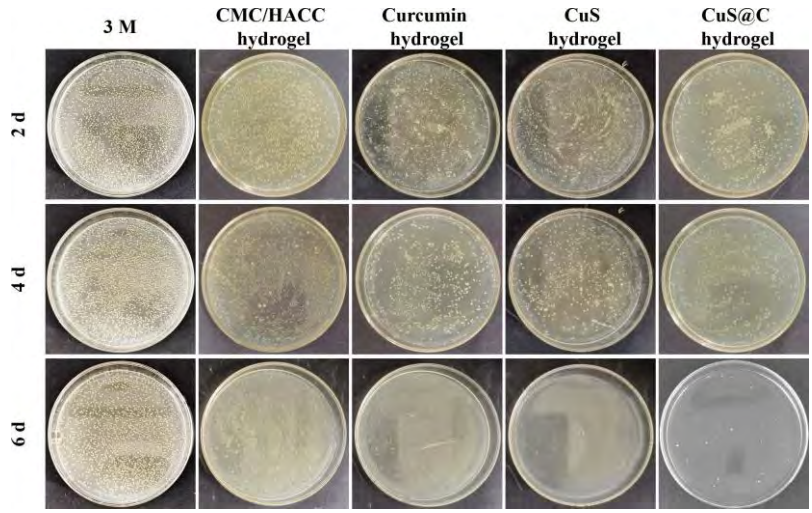


**Figure S16.** Photographs of *S. aureus* treated with hydrogels with or without 808 nm NIR irradiation *in vivo*.

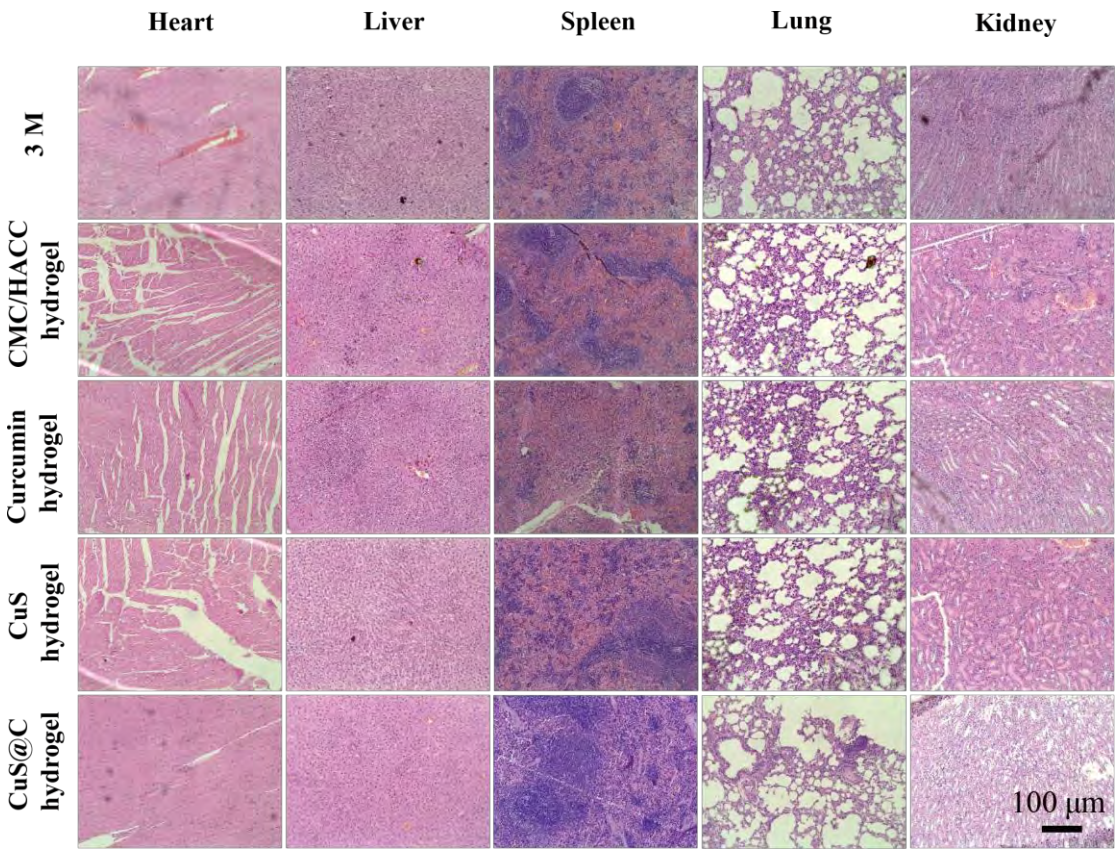


**Figure S17.** H&E staining of major organ tissues after 10-day treatment with different hydrogels.